Paper-based Analytical Devices with Integrated VLSI Potentiostat

A thesis submitted by

Meera Punjiya

In partial fulfillment of the requirements for the degree of

Master of Science

in

Electrical Engineering

Tufts University
August 2016

Thesis Advisor: Professor Sameer Sonkusale
Committee: Professor Xiaocheng Jiang and Professor Valencia Koomson

Abstract

There is a need for low cost, self-contained, point-of-care medical diagnostics for resource poor settings. Such diagnostics have the potential to greatly improve health outcomes through early detection and rapid diagnosis. Recently, paper based devices similar to paper strips in glucose meters have been demonstrated as a viable and low cost platform for diagnostics. In addition to being low cost, paper is easily transportable, biocompatible and can be safely disposed by incineration. Furthermore these paper-based sensors can be fabricated at room temperature using readily available and inexpensive equipment and materials, essential in regions with limited resources. Paper based devices which employ electrochemical sensing methods are the most sensitive class of these devices. Unfortunately, readout is traditionally completed with a benchtop potentiostat not suitable for portable applications. This thesis presents a CMOS readout IC with a VLSI potentiostat designed for sensing with paper-based electrochemical biosensors and a 3D electrochemical paper based analytical device suitable for multi-analyte detection. The platform is evaluated for dopamine and glucose sensing. Collectively, this work contributes to a portable low-cost diagnostics platform for use in resource scarce areas.

Acknowledgements

My sincere gratitude goes out to the numerous individuals who have made my graduate studies and this Thesis possible. First and foremost, I would like to thank my adviser, Professor Sameer Sonkusale for his mind-opening mentorship, extreme patience and constant encouragement. I would also like to thank my committee members, Dr. Valencia Koomson and Dr. Xiocheng Jaing. I appreciate your feedback, time and expertise.

A special thanks to Pooria Mostafalu, Robert D'Angelo, Saroj Rout, Chirag Sthalekar and Chung Hee Moon without whom little of the work would have been possible. I would also like to thank all of the current and former Nanolab and AICSL members.

And last but certainly not least, I would like to thank my family and friends for their everlasting support, even in my poorest of decisions. Mom, Dad, Julia, my wonderful roomies, my 200 BA crew and all my masis, masas, fois, fuvas and kakas, I am forever grateful for your incredible love and support.

Table of Contents

List of Tables

List of Figures

1 Introduction

1.1 Research Motivation and Background

Treatable diseases such as HIV, pneumonia, cholera, chlamydia and diabetes still plague much of the developing world despite advances in treatment of these diseases. The primary barrier to treating such diseases in developing countries where reliable power, refrigeration and sanitation are not available is lack of accessible health care and diagnostic tools [1]. The 1980s and 1990s saw the development of ultrasensitive analysis techniques such as PCR which could be used to screen for many infections in the developed world, thus leaving much of the developing world without effective diagnostic tools. [2]
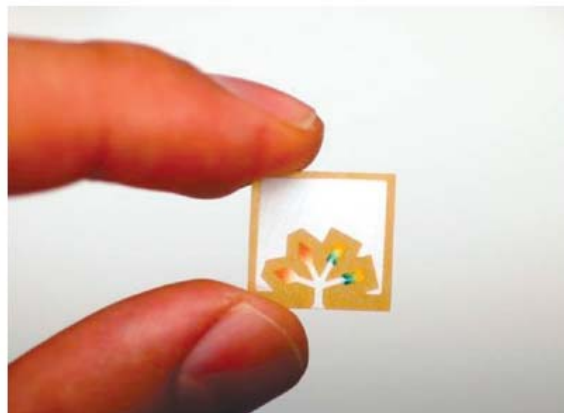
Figure 1.1: Colorimetric paper-based analytical device for detection of glucose, cholesterol and protein [1]

In 2004 the world health organization (WHO) reported that there was an "urgent need to further develop new diagnostic tools for [sexually transmitted infections] that are designed explicitly to address the needs and conditions of populations in the developing world, where the disease burden is clearly greatest".

[3]. They laid out requirements for usable diagnostic tests in these environments in their report stating that for tests to be usable, they must be ASSURED: affordable, sensitive, specific, user-friendly, rapid and robust, equipment free and delivered [3]. The past decade has thus seen a surge in development of devices of low-cost portable health screening devices.

To meet the ASSURED requirements, micro paper-based analytical devices (uPADs) were first developed by George Whitesides's research group at Harvard University in 2007 [1]. As required, these devices are cheap, require small volumes of analyte and little to no external equipment for measurement. One such device for the detection of glucose, cholesterol and protein is seen in Figure 1. As the name suggests, these devices are paper-based and use colorimetric or electrochemical means, known as electrochemical paper-based analytical devices (ePADs), to detect specific analytes. They can be 2D or 3D resulting from paper folding to realize more complex assays and structures.
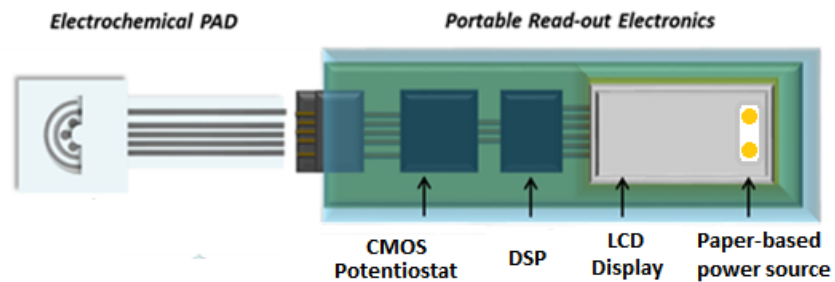
Figure 1.2: Graphical representation of portable diagnostics device

This thesis contributes a complementary metal-oxide-semiconductor integrated circuit (CMOS IC) with a VLSI potentiostat designed for sensing with paper-based electrochemical biosensors and a 3D electrochemical paper based analytical device suitable for multi-analyte detection. CMOS leverages the mature semiconductor industry to miniaturize the entire potentiostat operation to a single

2

chip, saving area, power and cost. Collectively, this work contributes to a portable low-cost diagnostics platform for use in resource scarce areas. One such representation of this device is shown in Figure 1.2. This chapter will briefly introduce paper-based analytical devices and the fundamentals of the electrochemical methods used for sensing from a specific subset of these devices (ePADs). An outline of this Thesis will be provided as the end of the chapter.

1.2 Paper-based analytical devices (PADs)

Paper-based analytical devices (PADs) have developed in the last decade to perform sophisticated analysis but have remained simple to use. Advances in fabrication technologies such as wax and 3D printing have allowed PADs to move beyond qualitative diagnosis, to complete complex functions such as timed delivery of reagents, signal amplification and blood separation [4].

Devices are typically fabricated using a simple clean room free process which involves creation of hydrophilic areas on a porous paper substrate using wax printing or deposition of another hydrophilic materials using screen printing to create microfluidic channels. Sensing materials are subsequently deposited onto the appropriate areas using a screen printing or drop-casting method [5].

Broadly, PADs can be divided into two categories, colorimetric and electrochemical PADs (ePADs). Colorimetric pads, such as that seen in Figure 1.1, rely on a color change for readout. This class of pads can include those where information is contained in the time between two color changes known as time-based pads [4]. Electrochemical PADs employ an electrochemical method for

3

readout. This can include amperometry, conductivity or voltammetry such as linear voltammetry, cyclic voltammetry, square wave voltammetry and differential pulse voltammetry. These methods are further discussed in the following section. Readout with these sensors requires a potentiostat to employ the appropriate electrochemical technique. Potentiostat design and function are future discussed in Section 2.1. These two dimensional pads can be easily extended to the third dimension by simple paper folding. The third dimension offers additional functionality such as multiple analyses to be conducted in parallel and mixing of analyte to occur only when the analysis is to occur. The detailed fabrication of PADs and applications are provided in Section 3.2.

1.3 Evolution of ePADs

Martinez *et al.* first fabricated the modern day paper-based analytical device in 2007 for sensing of proteins and glucose using colorimetric means with detection limits of 0.75mM and 5mM respectively [5]. In 2009, Dungchai *et al.* published the first electrochemical paper-based sensor, demonstrating that electrochemical sensing on paper substrates could provide greater sensitivity with glucose detection limits down to 0.7mM [6].
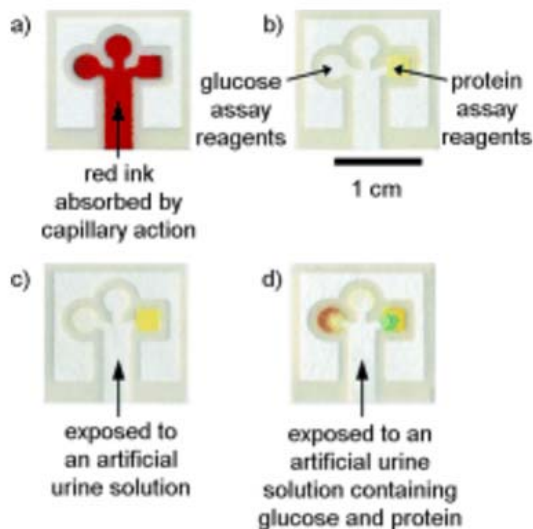
Figure 1.3: First Colorimetric PAD fabricated by [5]
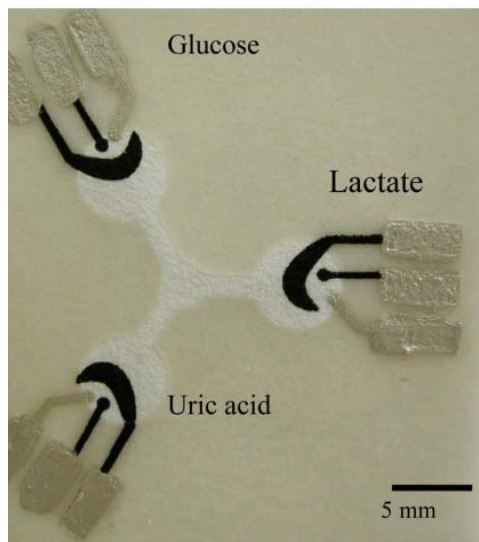
Figure 1.4: First Electrochemical PAD published by [6]

Electrochemical paper based sensors can now provide femtomolar sensing resolution and have been employed on PADS for the detection of antibodies, gases, metals, pH, and protein as well as for detection of physical parameters such as strain, force, temperature and humidity. A range of electrochemical techniques have been used for detection of analytes including measurement of relative resistivity, impedance, amperometry, conductivity and voltammetry [4]. The design by Dungchai et al. in 2009 used screen printing carbon and Ag/AgCl ink to create electrodes and were used with cyclic voltammetry and chronoamperometry for enzymatic detection of glucose, lactate and uric acid. The device demonstrated improved sensitivity and selectivity relative to colorimetric devices. Standard lithography was used to create hydrophobic regions on paper leaving a microfluidic channel. Wax patterning has since replaced this method of creating hydrophobic regions on chromatography paper. This method was first introducing by Lu *et al.* [7]. Paper was patterned with a commercial wax printer and heated to hydrophobic

5

barriers through the paper. The printed sensors was then functionalized with TMB and HRP for sensing of glucose.
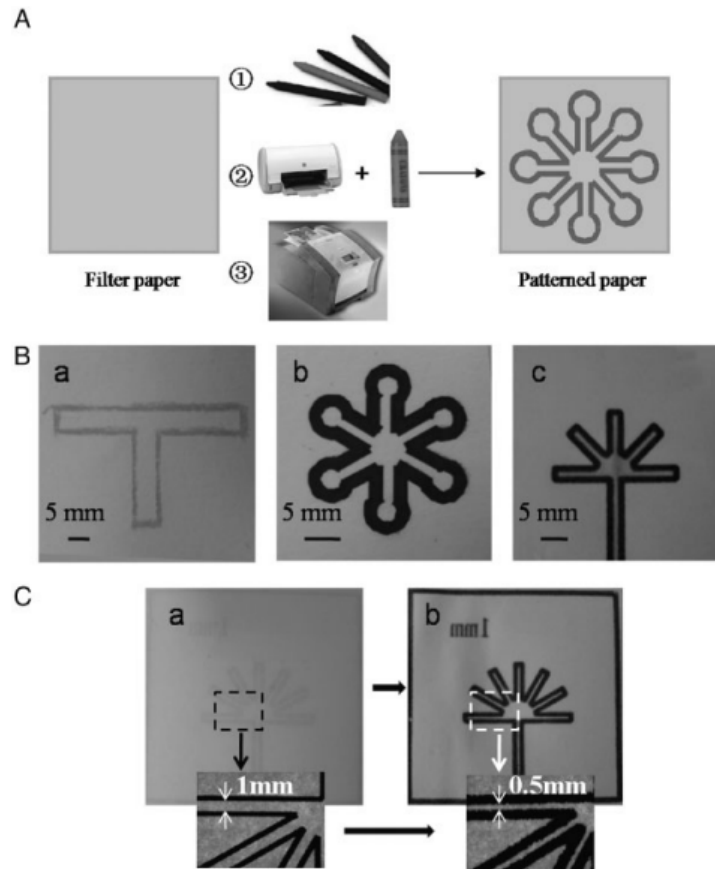
Figure 1.5: Wax patterning of paper using a commercial printer to create hydrophobic regions. [7]

1.3.1 3-Dimensional ePADs

Three dimensional pads were first fabricated by Martinez *et al.* in 2008 in conjunction with colorimetric sensing [8]. The devices, seen in Figure 1.6 below, stacked wax pattern paper to realize a 3D structure. Richard Crooks group at the University of Texas, Austin improved upon this design in 2011, using paper folding

or origami to realize a 3D structure [9]. They termed these devices oPADs seen in Figure 1.7 . 3D ePADs have since been used to detect DNA, heavy metals, small molecules, gasses, ions and proteins amongst other targets [4].
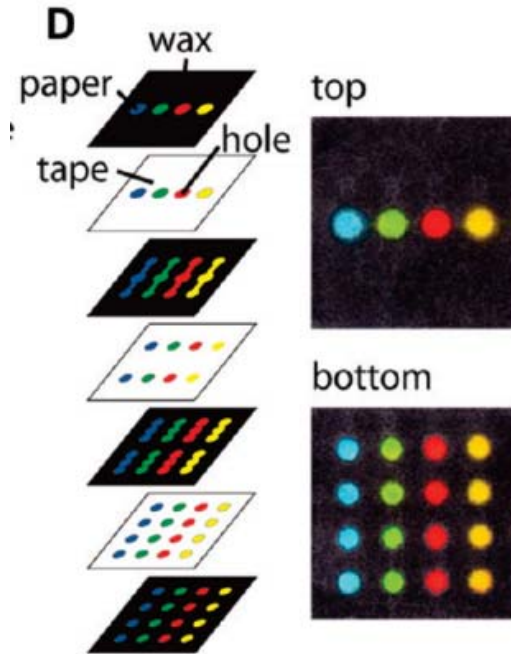
Figure 1.6: First 3D PAD fabricated by stacking paper and double-sided tape [8]

Fluidic channels created in paper-based devices, known as paper channels, are most commonly used to direct analyte in a PAD, however the there are three primary issues associated with paper channels. 1) The pore size in the substrate (~10um) can hinder the flow of micrometer scale objects. 2) The cellulose fibers can a nonspecific absorption due to their high surface area and 3, the rate of fluid flow is hindered by cellulose fibers, which may be beneficial in certain circumstances [9]. As a result, several works have focused on removal of cellulose fibers to create a hollow channel in 3D pads, seen in [10]. To realize hollow channels, cellulose can be removed from between wax printed regions using a laser cutter or a blade. With

stacking, a hollow channel can be created within the device. Hollow channels have been used to devices for the detection of small molecules, metal ions, ricin, DNA and BSA [4].
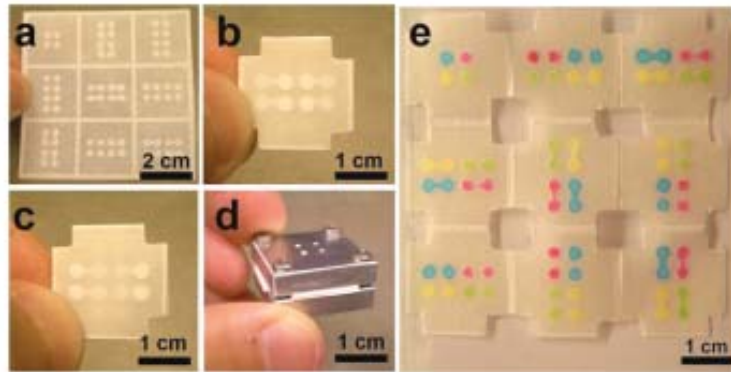
Figure 1.7: 3D PAD realized by folding of wax printed paper [9]
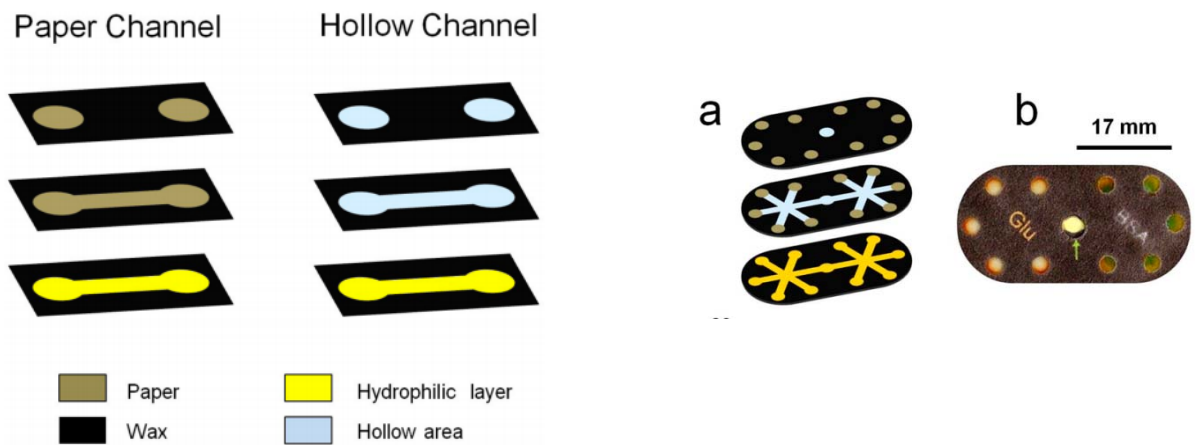
Figure 1.8: Hollow Channel PADs created by removing cellulose fibers in paper channels, first reported in [10]

1.4 Electrochemical Sensing Principles

In a typical electrochemical measurement, three electrodes, working (WE), reference (RE) and counter (CE), are immersed in a solution sample. Reference electrodes are commonly made from Ag/AgCl or calomel half cells. The role of the reference electrode is to maintain the potential of the working electrode. The CE provides a current which allows the redox couple in the solution to accept (donate) electrons from the CE and donate (accept) them to (at) the WE to maintain the potential difference between the WE and RE. Counter electrode, also called auxiliary electrodes, are large in surface area as to not be the limiting factor in a redox reaction rate [11].

In a redox reaction, the substances involved in the reaction change oxidation states either being oxidized or reduced. When a substance loses an electron, its oxidation state increases, thus it is oxidized. Conversely, when a substance gains an electron its oxidation state decreases and it is reduced. Redox reactions occur spontaneously when the Gibb's free energy for the electrochemical cell is negative. The Gibb's free energy for a thermodynamic system is given by equation (1) below and indicates the maximum work that can be completed by an isobaric (constant pressure) and isothermal (constant temperature) system. Here, n is the number of moles of electrons transferred in the reaction, F is faradays constant and E_{cell} is the potential difference between the anode and cathode in the electrochemical cell given by equation (2).

$$\Delta G = -nFE_{cell} \tag{1}$$

$$E_{cell} = E_{anode\ (CE)} - E_{cathode\ (WE)} \qquad \text{(2)}$$

Thus a redox reaction can be induced by changing the cell potential, E_{cell}. In the case of reversible reactions, the WE and CE can be either the anode or the cathode in the electrochemical reaction.

Varying E_{cell} and measuring the reaction rate (determined by the number of freed electrons) can provide valuable information about the type and quantity of species in the target analyte as well as the kinetics of the reaction [11]. These electroanalytical techniques can be broadly classified as voltammetric, amperometric or coulometric. Voltammetric techniques include, but are not limited to cyclic voltammetry, pulsed voltammetry and square-wave voltammetry. Amperometric techniques include chronoamperometry and pulsed amperometry. An outline of the classes of electrochemical techniques is provided in Figure 1.9.

A specialized instrument known as a *potentiostat* is used to implement these various electrochemical measurements. The general potentiostat seen in Figure 2.2 can be used for readout with amperometric electrochemical sensors via several analytical methods. The three methods employed in this work, cyclic voltammetry, chronoamperometry and potentiometry and are described in detail in the following sections.

```
                    interfacial
              electrochemical techniques

      static techniques              dynamic techniques
          (i = 0)                        (i ≠ 0)

      potentiometry          controlled              controlled
       measure E             potential                current

                      variable        fixed      controlled-current
                      potential      potential       coulometry
                                                    measure i vs. t

                              amperometry    controlled-potential
                               measure i         coulometry
                                               measure i vs. t

                  stirred              quiescent
                  solution   stripping  solution
                            voltammetry
                            measure i vs. E
      hydrodynamic
      voltammetry
      measure i vs. E

      linear potential        pulsed potential       cyclical potential
      polarography and        pulse polarography          cyclic
      stationary electrode    and voltammetry          voltammetry
      voltammetry             measure i vs. E          measure i vs. E
      measure i vs. E
```

Figure 1.9: Electroanalytical Technique Classes [12]

1.4.1 Cyclic Voltammetry

Cyclic Voltammetry (CV) is one of the most commonly used electroanalytical techniques because it provides information about both the kinetic and thermodynamic properties of chemical systems [11]. CV can be used to characterize electrochemically reversible systems. A typical CV setup uses three electrodes, a counter electrode, a working electrode and a reference electrode which are immersed in a liquid.

11

Cyclic Voltammagram Excitation Signal

Cyclic Voltammagram
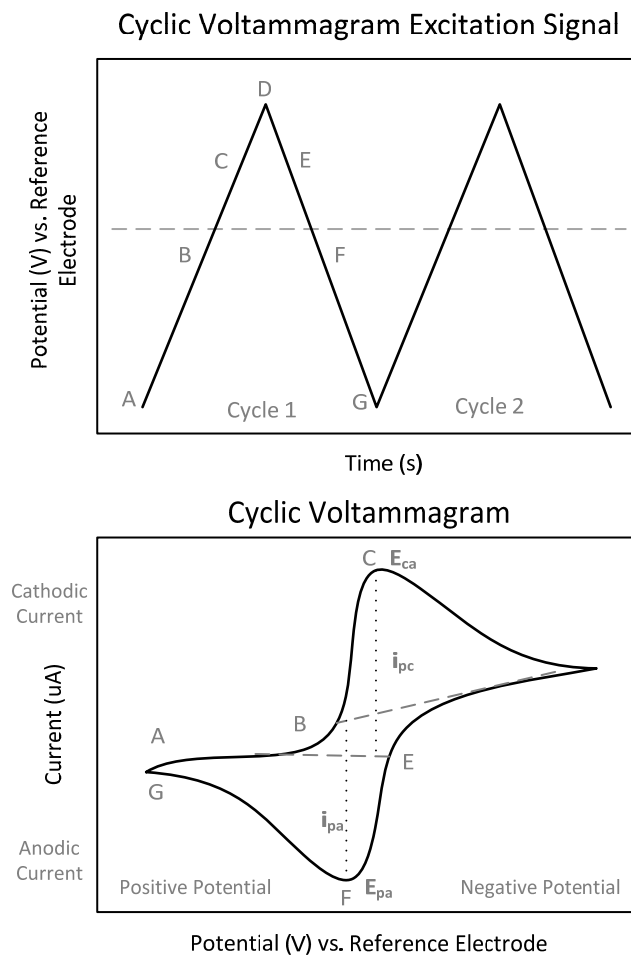
Figure 1.10: Cyclic voltammetry excitation waveform (top) and resulting cyclic voltammagram (bottom). E_{pa} and E_{pc} indicate the locations where the peak anodic current (i_{pa}) and peak cathodic current (i_{pc}) occur respectively [13].

CV, which is only valid for reversible chemical processes, applies a triangular excitation waveform to the counter electrode which initiates an oxidation (reduction) reaction at the counter electrode and a reduction (oxidation) reaction at the working electrode. Current is measured at the WE and plotted against the applied potential to determine the resulting cyclic voltammagram for the measurement, seen in Figure 1.10. The measured current is dependent on two processes, the movement of the electroactive material to the surface of the WE and the electron transfer rate for the given redox reaction [14].

12

The excitation waveform for a typical CV measurement is shown in the top panel of Figure 1.10 for two cycles. A typical resulting current measurement in shown in the bottom panel of Figure 1.10. Here, i_{pa} and i_{pc} indicate the peak anodic and cathodic currents respectively and E_{pa} and E_{pc} indicate the potential at which these peak currents occur. The peak currents' relationship to the concentration of analyte in the solution is given by the Randles-Sevcik equation (3) where n is the number of electros transferred per molecule, A is surface area of the electrode, D_o is the diffusion rate, v is the CV scan rate and C_o^* is the bulk solution analyte concentration.

$$i_P = 0.4463nFAC_0^* \sqrt{\frac{nFvD_0}{RT}} \tag{3}$$

1.4.2 Chronoamperometry
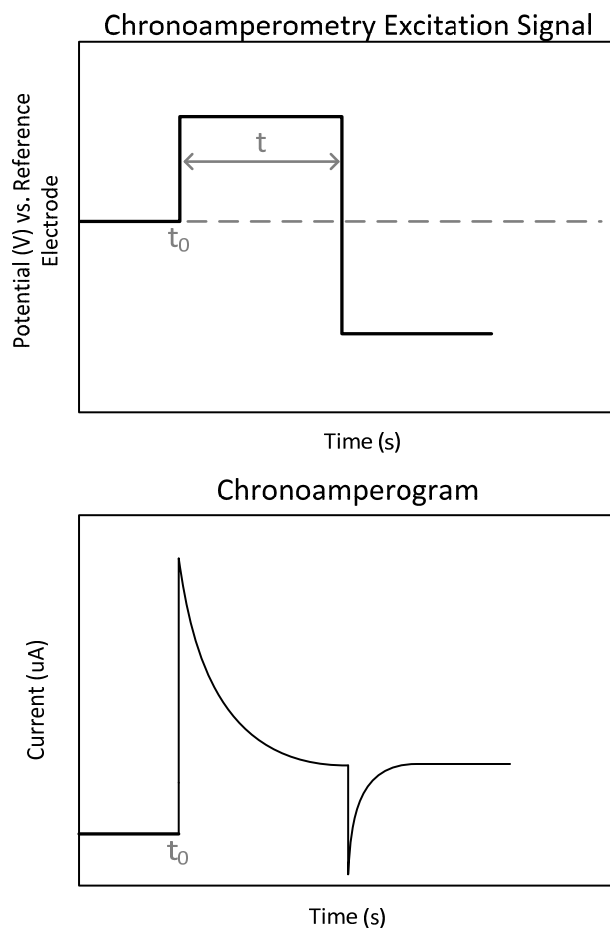
Figure 1.11: Chronoamperometry excitation waveform (top) and resulting Chronoamperogram (bottom). The time since redox potential is applied is indicated by t and is relative to t_0.

Chronoamperometry examines the step response of an electrochemical system. A potential step at the working electrode exceeding the redox potential induces an electrochemical reaction which causes a change in measured current with time until the system reaches equilibrium. The examination of this current response with respect to time is known as chronoamperometry. This electrochemical technique relies on rate of diffusion of analyte to the electrodes

14

surface and thus the solution must be left undisturbed for a valid measurement [15]. In this reaction, the current at the working electrode is governed by the Cottrell equation (4), which relates the resulting current to the concentration of analyte in the bulk solution.

$$i(t) = \frac{nFAC_0^*\sqrt{D_0}}{\sqrt{\pi t}} \qquad (4)$$

Here n is the number of freed electrons, F is faradays constant, A is the area of the electrode, D is the diffusion rate, C_0^* is the bulk analyte concentration and t is the time since the applied step [15]. When determining analyte concentration using this method, it is important to us a time point in the later 70-80% of the scan to allow the capacitive current to decay [16]. The excitation waveform and resulting chronomperogram are shown in Figure 1.11.

1.4.3 Potentiometry

Unlike the previously described amperometric and voltammetric techniques which measure current to determine system properties, in potentiometry the potential of an electrode in an electrochemical cell is measured to determine the concentration of ions in a solution. This measurement typically only requires two electrodes, a reference electrode and the working electrode.

The potential of a solid state electrode is given by the Nernst equation (5). As is evident, the electrode potential is dependent on the temperature of the solution as well as the concentration of the ions in the solution.

15

$$E = E_0 - \frac{RT}{nF}\ln(a) \tag{5}$$

In the Nernst equation, E_0 is the standard electrode potential, R is the universal gas constant, T is the temperature of the solution/electrode, n is the number of moles of electrons transferred, F is Faraday's constant and a is the ion activity; when ion concentration is less than 100mM, the ion activity can be approximated as concentration. Thus there is a logarithmic relationship between the measured electrode potential and the concentration of ions in the bulk analyte solution.

1.5 Thesis Overview

This thesis is segmented into three parts which describe the two components of the low-cost portable diagnostics system. Chapter 2 describes the design of the CMOS readout IC implementing a potentiostat and dual slope ADC. The IC is custom designed for sensing with various paper-based sensors. The first part of this chapter outlines the target specifications for the potentiostat which is followed by the chosen topology. The core of the potentiostat is a class-AB buffer amplifier and a variable gain TIA realized by connecting the amplifer in feedback with a variable resistor bank. The electrical performance of the fabricated IC is provided in this chapter. Chapter 3 describes the design and fabrications of ePADs for sensing of dopamine and glucose and measurement of pH. The first part of this chapter briefly explains the sensing mechanism. Two ePAD designs using for sensing are presented in this chapter: a single-analyte ePAD used for dopamine sensing and a 3D origami ePAD used for dopamine and glucose sensing. An in-depth explanation

of fabrication and sensor design is provided in this chapter. Chapter 4 includes the results of sensing glucose and dopamine with the fabricated ePADs in conjunction with the fabricated IC. Test setups and procedures are provided in this chapter. A conclusion and a summary of future work is provided in Chapter 5.

2 CMOS Potentiostat Readout IC Design

This chapter describes the design of a CMOS potentiostat readout IC for electrochemical sensing measurements using electrochemical paper-based analytical devices for low-cost diagnostics. The goal of this work was to develop a miniaturized and portable potentiostat for sensing with electrochemical PADs using multiple electrochemical techniques. A possible implementation of this potentiostat in a resource scarce environment is provided in Figure 1.2.

The readout IC is designed in a 0.18um process node and contains a full single channel potentiostat as well as a dual-slope ADC both of which can be used in isolation. The first part of this chapter describes potentiostat operation and the specifications for such an instrument. The second part describes describes in more detail the design and operation of the CMOS potentiostat readout IC and each of the system blocks including a class-AB amplifier, a variable gain TIA and a dual-slope ADC. The amplifiers and ADC are described and analyzed in this portion along with the results of electrical testing and simulation.

2.1 Potentiostat Operation and Specifications

A potentiostat is a specialized instrument used to take measurements with electrochemical sensors. In amperometric techniques, the primary purpose of a potentiostat is to control the potential of the counter electrode with respect to the reference electrode so that the potential between the WE and the RE corresponds to that desired by the user while simultaneously measuring current from the WE.

There are several commercial bench top potentiostats available on the market. Once such instruments, manufactured by Gamry Instuments is provided in Figure 2.1 for illustrative purposes. The primary problem with these instruments for portable applications in resource scare environments is that they are large and require a significant amount of power. The goal of this work was to develop a miniaturized and portable potentiostat for sensing with electrochemical PADs using multiple electrochemical techniques. We leveraged the maturity and yield of the commercial semiconductor CMOS foundry to realize a miniaturized single chip potentiostat, which saves area, cost and power and is much more amenable to deployment in the developing world.

Figure 2.1: Commercially available potentiostat sold by Gamry [17]

Simply a potentiostat for amperometry and voltammetry can be realized using two amplifiers, a control amplifier and a transimpedance amplifier as seen in Figure 2.2. The control amplifier must be capable of driving the low resistive loads associated with highly conductive electrolytes and must have an output dynamic range capable of driving the CE with the necessary redox potential for the species under test. The transimpedance amplifier here is used to measure current from the working electrode. The transimpedance amplifier can be replaced with any circuitry

capable of converting the resulting electrode current. Previous work has included direct digitization of resulting current via an integrating ADC [18], conversion to frequency [19] , and conversion to time [20].
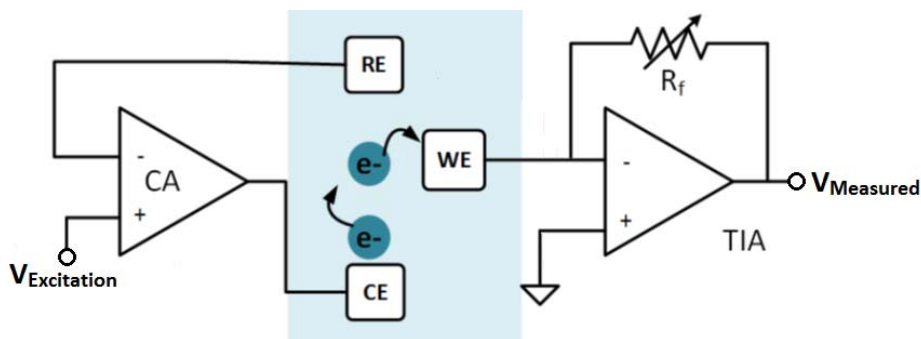
Figure 2.2: Simple Realization of a Potentiostat using Operational Amplifiers

For this work, an output swing of at least 1V was desired. This was determined by the oxidation reduction potential of platinum (+1.2V), a common counter electrode material, with respect to Ag/AgCl, commonly used a reference electrode (+.22V) [21], [22]. A wealth of sources have demonstrated sensing of dopamine, ascorbic acid, uric acid, glucose and lactose using platinum counter electrodes with carbon based electrodes [23]. The CO2/C redox couple (+.287V) present at the surface of the carbon electrodes has a lower oxidation reduction potential with respect to Ag/AgCl and thus, a 1V swing was deemed sufficient.

The resulting current from the electrochemical measurement is highly dependent on the electrode surface area. To accommodate a number electrode types and sizes as to not limit the applications of the potentiostat, it was desirable to measure currents from screen-printed microelectrodes with current magnitudes on the order of hundreds of nano-amperes [24] to hundreds of micro-amperes, possible

from macro-sized screen printed electrochemical sensors [25]. While not a primary requirement, it was also desirable to maintain a relatively low power consumption. There are obvious limitations to the power source for a portable potentiostat. A reasonable expectation was to keep static power consumption below 2mA.

2.2 Electrochemical cell model

A critical component of the readout electronics design was creation of a good electrical model for the paper based electrodes. The parasitic resistances and capacitances associated with the devices can affect the stability of the electronics and must accurately be modeled for consideration in the design process. Electrical impedance spectroscopy data was collected to

Electrical impedance spectroscopy (EIS) is commonly used to create electrical equivalent models for electrochemical cells. In EIS, impedance measurements are taken for the electrode at various frequencies. Electrode parameters can be extracted by fitting the obtained data to a circuit model. The simplest of these is the Randles model seen in Figure 2.3 below [26].
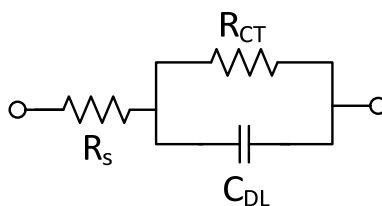
Figure 2.3: Randles Electrode Model [26]

Here, C_{DL} models the double layer capacitance, R_{CT} the charge transfer resistance and R_S is the solution or analyte resistance [26]. There are several models

for the formation of an EDL on an electrode surface. Simply, double layer capacitance is the result of an electric double layer (EDL) which forms from charge adsorption that occurs on the surface of the electrode which collects near the surface and attracts ions of opposite polarity rendering a capacitance as illustrated in Figure 2.4 [27].
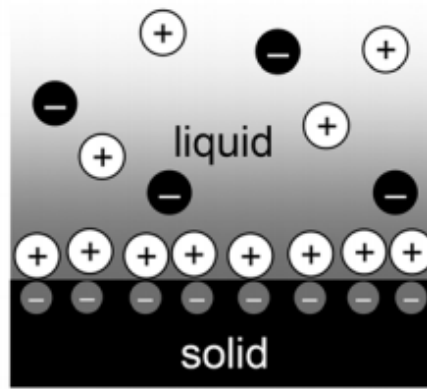
Figure 2.4: Electrical double layer capacitance formation in solid state electrodes immersed in ionic liquid [27].

The charge transfer resistance models the time and energy for charge transfer required at the surface of the electrode. The values of R_{CT} and C_{DL} will vary greatly depending on electrode material and the analyte used. Values for these model components were extracted from various sources in the literature and are provided in Table 1.

Table 1: Randles model values for various electrode materials

Electrode Material	R_{CT} Ω/cm^2	R_S Ω/cm^2	C_{DL} nF/cm^2	Source
Pt	4.48×10^5	28.0 (Neuron Medium)	-	[28]
Glassy Carbon	171	13.6 (Buffer Acetate)	5.1	[29]
Carbon Paste	189	24.4 (10g/L Fe^{2+} ions)	68.4	[30]
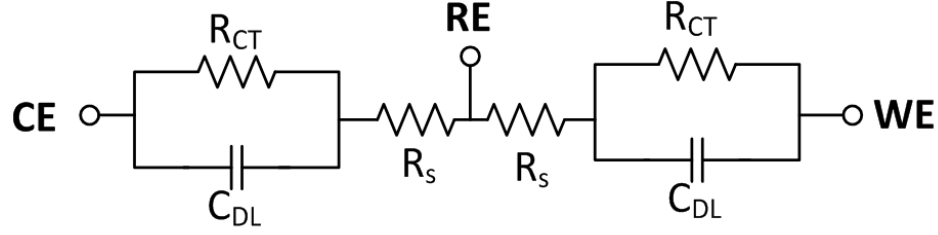
Figure 2.5: Electrical circuit used for modeling of 3-electrode electrochemical cell

2.3 CMOS IC Topology

A CMOS potentiostat readout IC was designed in a 0.18μm process for sensing with fabricated ePADs. An overview of the IC is provided in Figure 2.6. To meet the previously described potentiostat specifications while still maintaining a reasonable DC power consumption for a portable device, a class AB buffer-amplifier, seen in Figure 2.7, was designed and implemented on the CMOS potentiostat readout IC. This buffer-amplifier is a fully symmetrical version of the class AB buffer-amplifier proposed by You *et al.* [31] and was designed in a 0.18μm process. The class AB output stage employs adaptive loads to provide process independent quiescent current control and was selected for its increased output dynamic range compared to previous class AB buffer designs [11]. The utility and design of this amplifier are further described in Section 2.4.

This class AB amplifier was used in feedback with an on-chip resistor bank to realize a transimpedance amplifier. The resistor bank allows for adjustable transimpedances of 5k, 50k, 100k and 500k to accommodate the currents generated by multiple electrode sizes. For digitization, a dual-slope ADC was implemented and is described in detail in Section 2.6. The dual-slope ADC was advantageous for this application due to its high linearity and achievable resolution and small
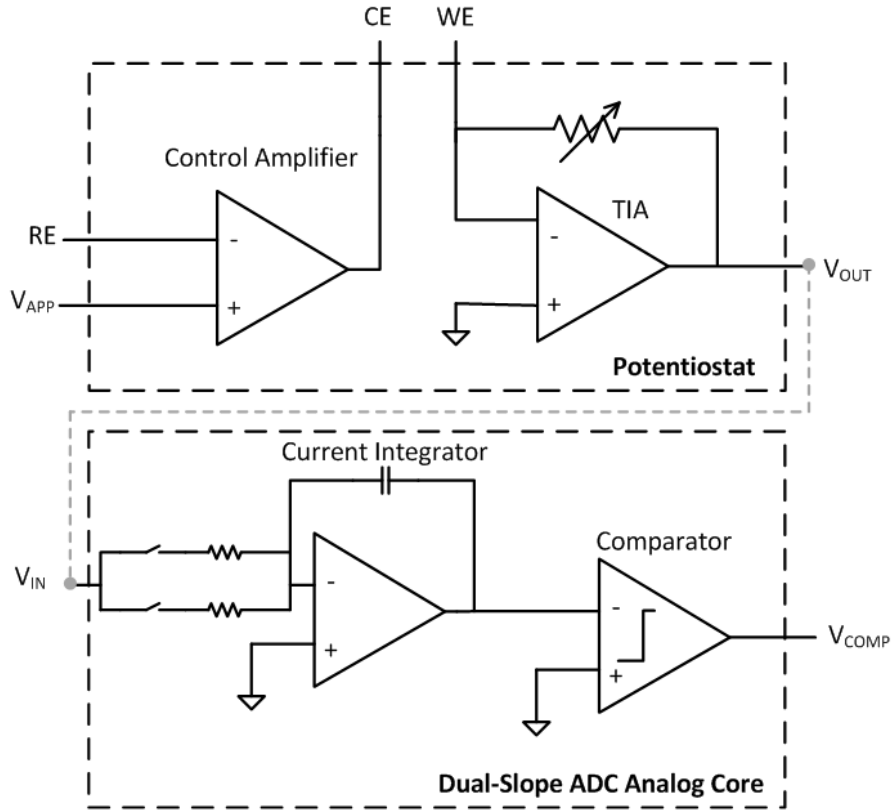
Figure 2.6: CMOS Potentiostat Readout IC Block Diagram

footprint. The core analog components of the dual-slope ADC were implemented on-chip and was to be interfaced with an FPGA for realization of the full ADC.

2.4 Class AB amplifier design

Class AB buffers are commonly used for their high current drive capability which allows them to drive small resistive loads while maintaining a low quiescent power consumption and low distortion compared to class B designs. Thus Class AB buffers are ideal for portable applications where power consumption is a limitation [31].

The class AB design implemented for this application is seen in Figure 2.7 and is adapted from the design first proposed by You *et al.* [31]. The design provides process independent quiescent current control. The core of the class AB buffer-amplifier is a standard cascoded two-stage OTA which uses a differential pair input stage and was design for a 63B gain and 60° phase margin. P-channel inputs were chosen to reduce 1/f noise [32]. The class AB stage utilizes adaptive loads to achieve stable quiescent current, independent of process variations. Under quiescent conditions the loading at nodes A and B is small; the adaptive loads M12/M11 and M13/M14 are in saturation with an ids of ~3uA. The loads provide stable quiescent current due to gain reduction of the intermediate inverting stages at the quiescent operating point. The compensation scheme outlined by Pernici *et al*. was used to stabilize the class AB buffer amplifier [33].
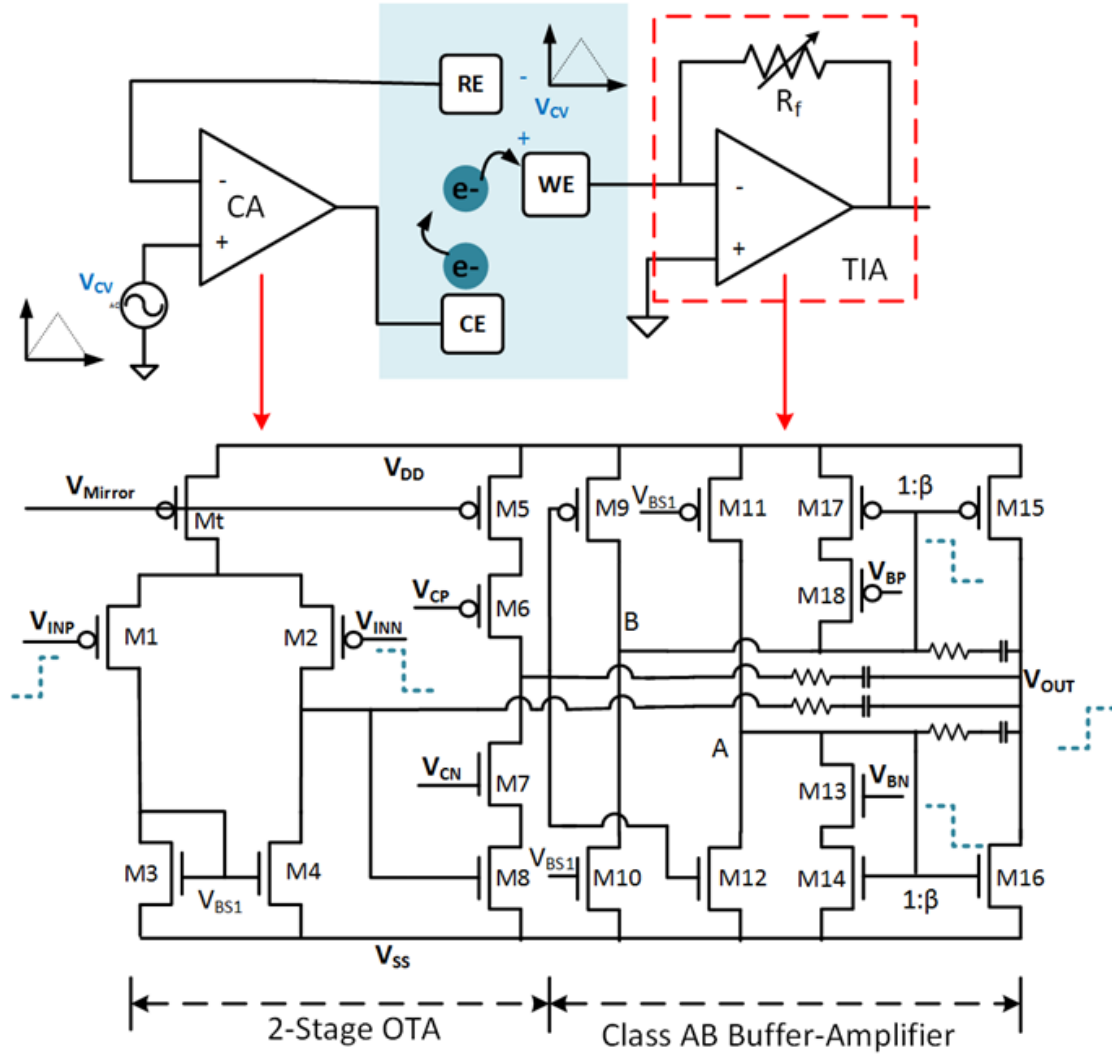
Figure 2.7: Designed Class AB Buffer-Amplifier

During transient operation, transistors M7 and M8 are pulled out of saturation, increasing their effective loading allowing the swing at nodes A and B to be large enough to provide maximum drive for M15 and M16.

The amplifier was designed with a nominal quiescent current of 160uA. With adaptive loads, Monte Carlo simulations of the amplifier show a 31.15% standard deviation in output quiescent current from the mean with mismatch for 200 runs; the same value without the adaptive loads increases to 56.63%. The simulated output quiescent current and their distributions for the two cases are seen the histograms in Figure 2.9 and Figure 2.8.
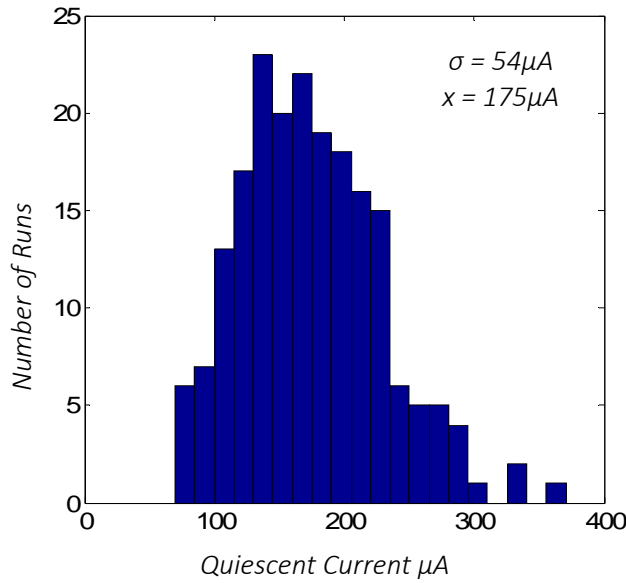
Figure 2.8: Histogram of Quiescent Current for Class AB buffer with adaptive loads
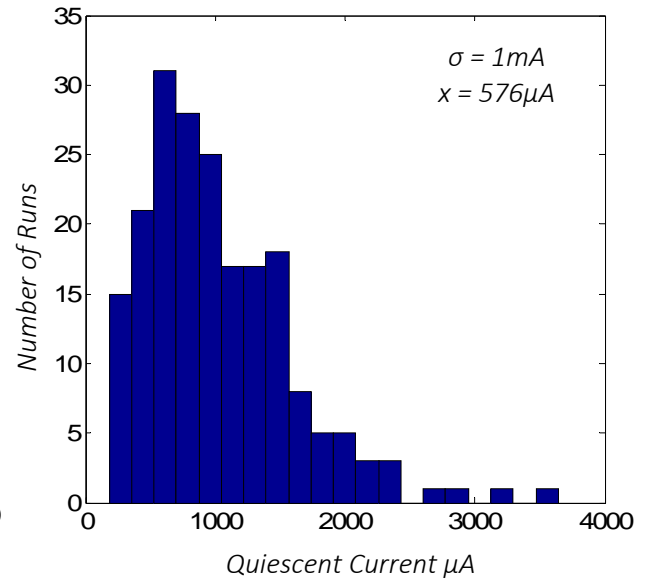
Figure 2.9: Histogram of Quiescent Current for Class AB buffer without adaptive loads

Device sizes for the final AB are tabulated below. Measurement schemes and associated simulation data are explained and analyzed in further detail in Appendix A: Class AB Amplifier Simulation. The buffer is capable of sourcing up to 24mA and sinking 13mA. And maintains a 1.6V output swing while driving a 200Ω load. The simulated class AB amplifier specifications are provided in

Table 3 below. While the 3dB bandwidth is low, this is sufficient for the application at hand. Future improvements to this amplifier design are further discussed in Section 0.

Table 2: Device sizes for Class-AB Buffer Amplifier seen in Figure 12

Device	Size	Device	Size
M1/M2	100/.32	M10	4.8/.6
M3/M4	20/3.2	M11	3.7/.6
M5	50/.32	M12	1.38/.6
M6	50/.32	M13/M14	4/.6
M7	9/.32	M15	360/.6
M8	9/.32	M16	55/.6
M9	10/.6	M17/M18	.6/.6

Table 3: Class AB Amplifier Specifications

Specification	Simulated (*Measured*) Value
Supply	2.5V
Process	.18μm
Static Power	1.5mW *(1.32mA)*
Buffer Quiescent Current	160uA
DC Gain	146 dB, (>73db for $R_{LOAD} > 10\Omega$)
3dB Bandwidth	3.3 Hz
UGF	12.73 MHz *(3.2MHz)*
CMRR	113.3 dB
PSRR	-65.3 dB
Integrated Input Referred Voltage Noise ($10e^{-6}$ to GBW)	53uV$_{RMS}$ *(47uV$_{RMS}$)*
Swing (200Ω,10k load)	1.6V, 2V *(2V, 1k load)*

2.5 Variable-Gain Transimpedance Amplifier

As discussed in Section 2.1, ideally the transimpedance amplifier would be capable of measuring currents from tens of nano-amperes to hundreds of micro-amperes. Realizing this dynamic range with a single feedback resistor, while possible, would

require an ADC resolution of 14 bits as determined in the derivation provided in Appendix B: Class-AB Amplifier Noise Requirements for TIA.

To relax this requirement, the transimpedance amplifier is realized by connecting a resistor bank in feedback with the designed op-amp. This additionally results in a relaxed input referred voltage noise requirement as well. The resistor bank contains 4 nominal value resistors of 5kΩ, 100kΩ, 50kΩ, 500kΩ. The bank is connected in feedback with the class-AB amplifier using the structure in Figure 2.10b. Gains are selected via a simple decoder and 2 bit selection input (*sel*) seen in Figure 2.10a. The input current range for the four transimpedances are provided in Table 4 along with the corresponding input referred current noise. Plots of the output voltage vs. input current from which these values are extracted can be found in Appendix C: Variable Gain TIA Transimpedance Measurement.
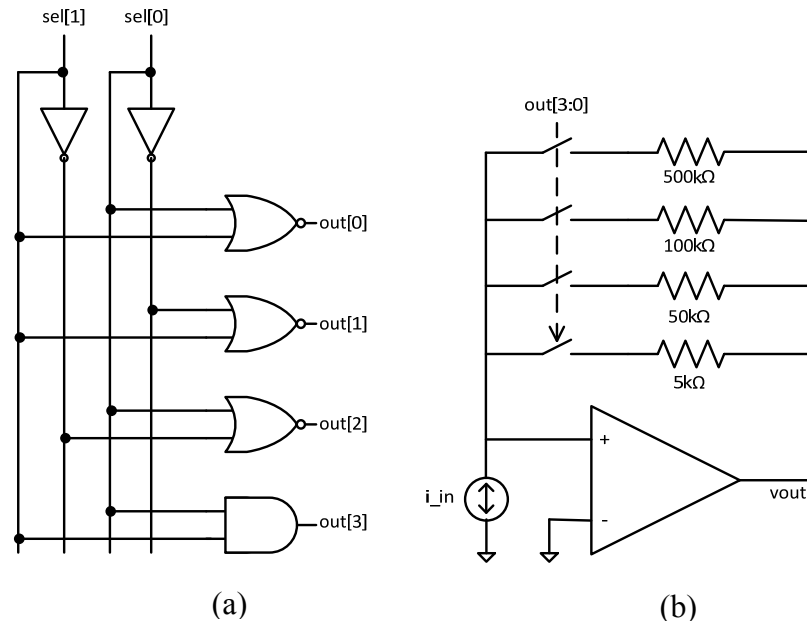
Figure 2.10: Transimpedance amplifier structure (right) and associated selection circuitry (left)

Table 4: Extracted Transimpedances for Variable Gain TIA

Selection (sel[1:0])	Transimpedance	Measured Transimpedance	Input Range	*Input referred current noise (simulated)*
00	5k	5856	-170uA - 170uA	7.5nA$_{RMS}$
01	50k	54269	-18.4uA – 18.4uA	2.043nA$_{RMS}$
10	100k	106257	-9.4uA – 9.4uA	1.43nA$_{RMS}$
11	500k	530567	-1.9uA – 1.9uA	.82nA$_{RMS}$
Dynamic Range		106dBΩ		

2.6 Dual-Slope ADC

2.6.1 Integrating ADCs

Integrating ADCs can provide superior noise and line frequency rejection and higher resolution compared to other converter types when high bandwidth is not required. Because these converters require relatively low power consumption they are often used in portable instrument applications such as digital multimeters.

Integrating ADCs include single-slope, dual-slope and multi-slope integrating ADCs. The primary components of integrating ADCs are a current integrator and a comparator. The single slope ADC measures the time is takes for an integrated value to discharge. The resulting output is related to this input by the RC time constant.

The dual-slope ADC improves on this design by making the final value insensitive to component value variation. A dual slope ADC was implemented on the potentiostat IC for its low power consumption, good noise rejection and high resolution.

2.6.2 Dual Slope ADC Design

As previously mentioned, the dual slope ADC relies on a current integrator with a counter and comparator to realize a simple ADC. The operating principle is outlined in Figure 2.11 with a simplified architecture in Figure 2.12 . The ADC has two phases of operation, a charging phase, where the input voltage (V_{IN}) is used to charge the capacitor on the current integrator for a known period of time and a discharge phase where the capacitor is discharged for an unknown time using a fixed voltage (V_{REF}). Measurement of this discharge time allows for quantification of the input voltage.

During the charging phase, V_{OUT} is given by (7). During the discharging phase, V_{OUT} is related to the discharge time (T_{DIS}) by (6). In both relationships, V_{IN} is the input voltage, V_{CM} is the common mode voltage, T_{CH} is the charge phase time, T_{DIS} is the time required to discharge the capacitor to V_{CM}, R is the integrator resistance and C is the integrator capacitance.

$$V_{OUT_{CH}} = \frac{V_{CM} - V_{IN}}{RC} T_{CH} + V_{CM} \tag{7}$$

$$V_{CM} = \frac{V_{CM} - V_{REF}}{RC} T_{DIS} + V_{OUT\_CH} \tag{6}$$

Solving for V_{OUT_CH} in equation 2 and substituting into 1 yields the final relationship between input voltage and the measured discharge time, given by (8)

$$V_{in} = (V_{CM} - V_{REF})\left(\frac{T_{DIS}}{T_{CH}}\right) + V_{CM} \qquad (8)$$
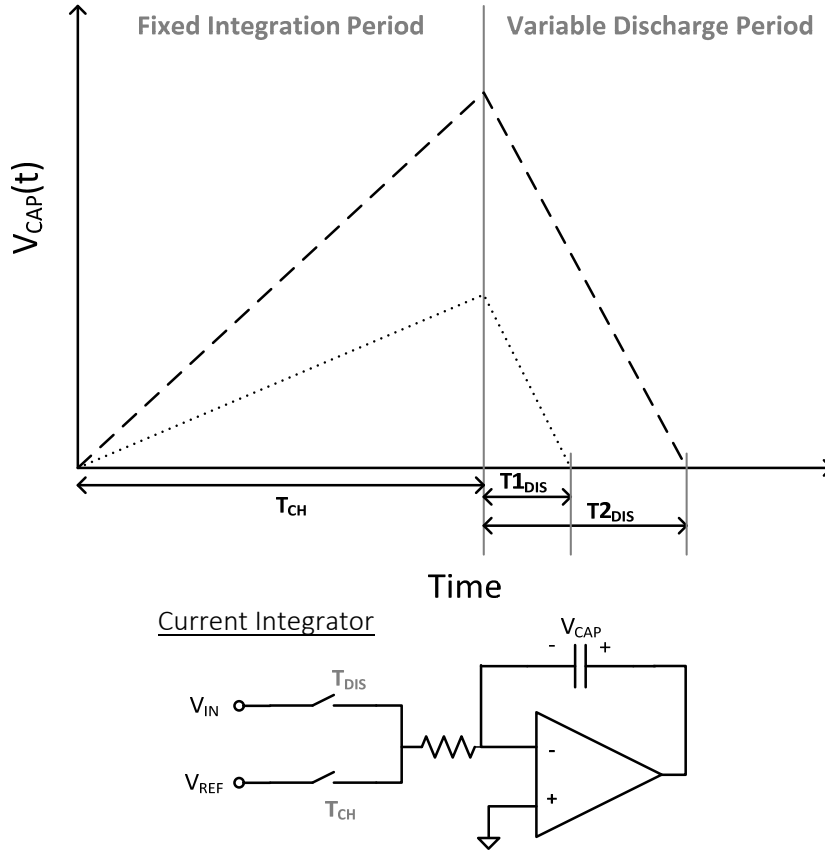
Figure 2.11: Dual Slope ADC Charge Integration Principle

As shown in Figure 2.12, measurement of this discharge time can be completed simply using a counter; a TDC can be used for greater timing resolution. For the complete architecture, digital control logic is needed to reset the current integrator and set the D flip-flops which hold the final digitized value. For digitization of values both above and below the common mode value of the implemented opamp, two current integrators and comparators are required for the complete structure seen in Figure 2.13.
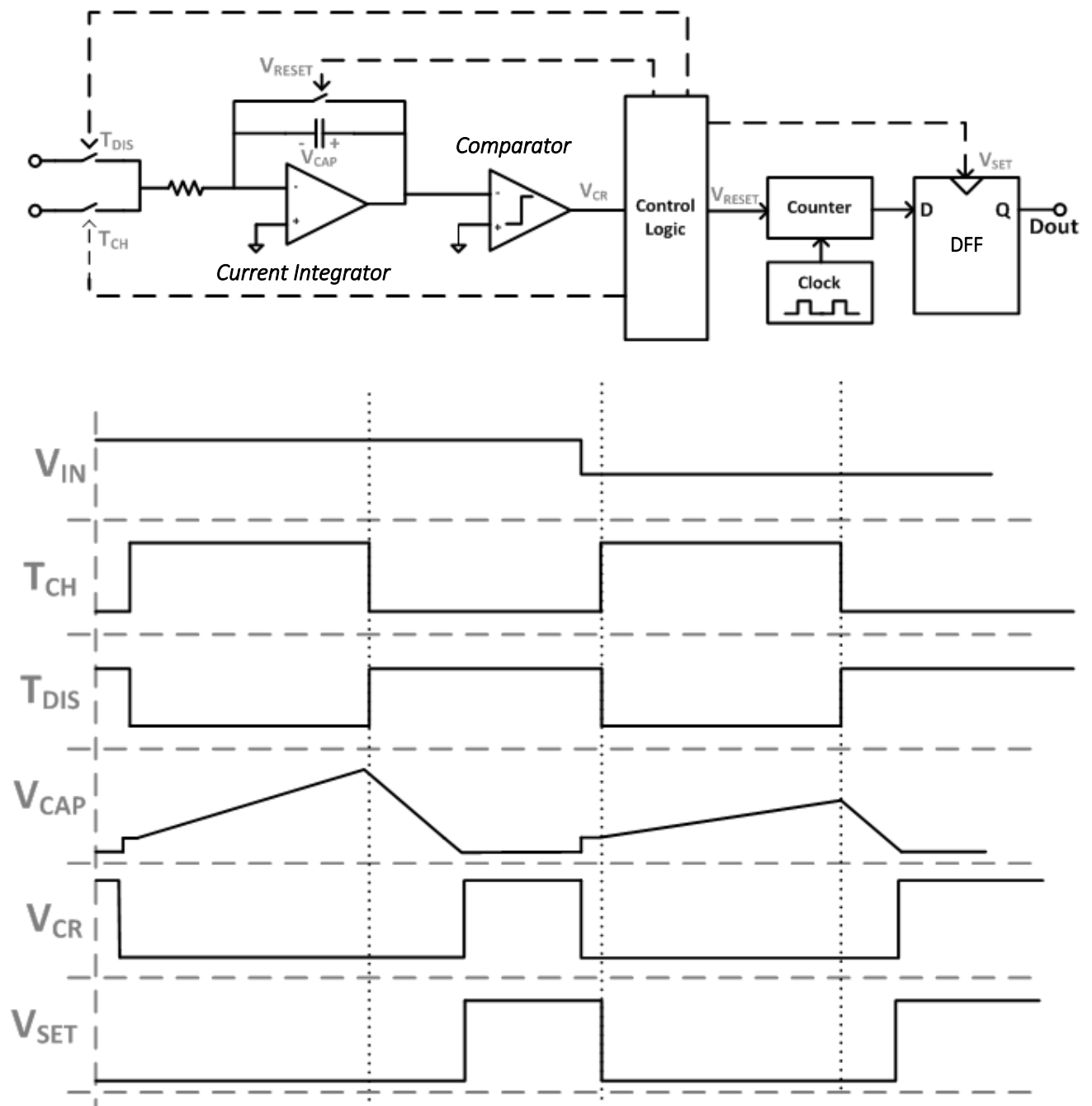
Figure 2.12: Simplified Dual-Slope ADC Architecture
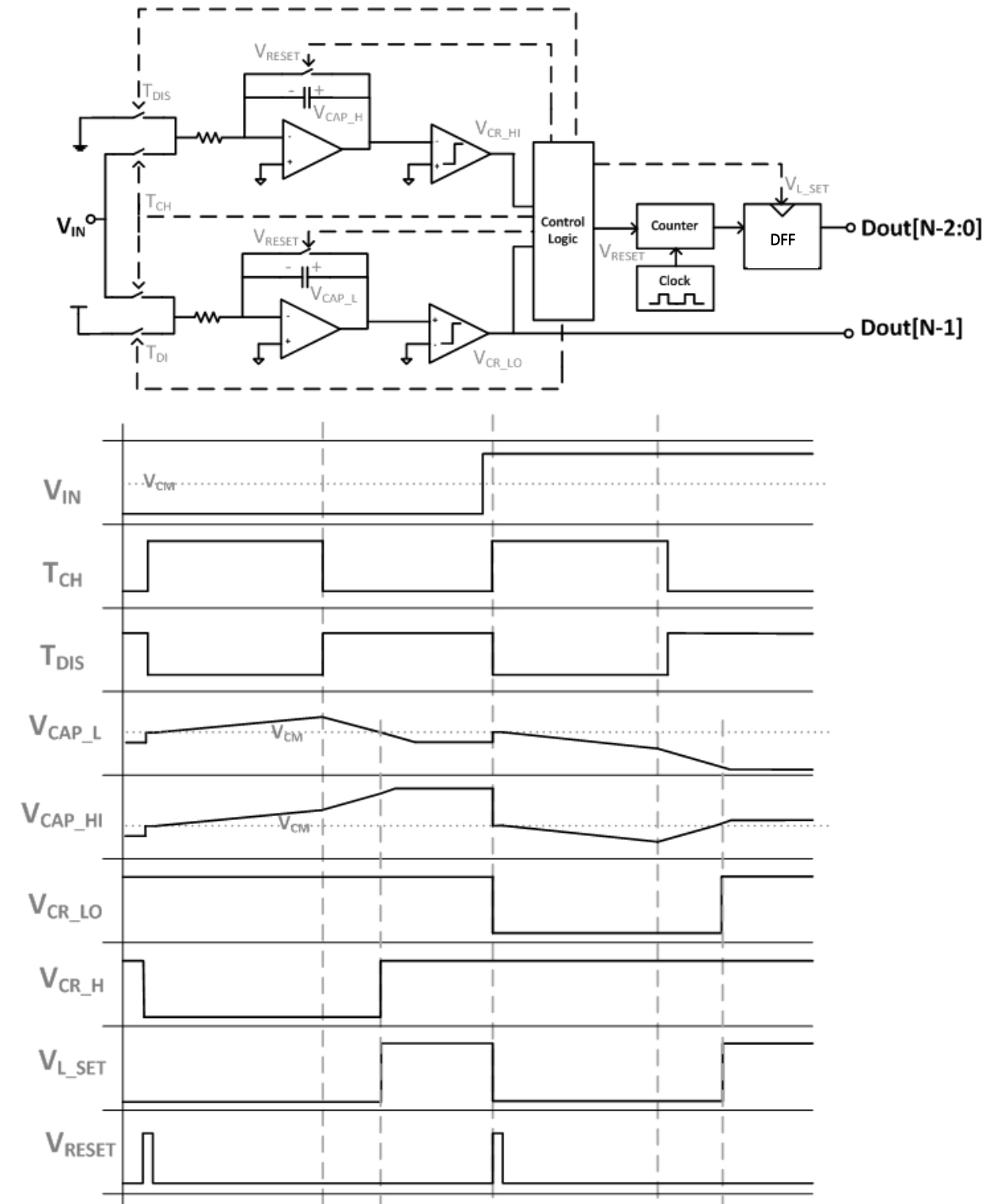
Figure 2.13: Complete Dual-Slope ADC Architecture

Here the top current integrator and comparator capture input voltages larger than the input common mode while the bottom set captures input voltages below the input common mode of 1.25V. In this implementation, the digital output has a signed representation where the sign bit is set by V_{CR_LOW}, the output of the lower comparator branch.

The simulated transfer curve for the complete architecture of Figure 2.13 is provided in Figure 2.14. The gain error and offset error for this dual-slope ADC structure are tabulated in Table 5. For simulation, Verilog-a behavioral models for the counter and logic gates were used. On the CMOS potentiostat readout IC only the current integrator and comparator of one branch of ADC was included for digitization of values above the common mode. This circuitry was to be interfaced with an FPGA to realize the full ADC. Simulated specifications for the design dual-
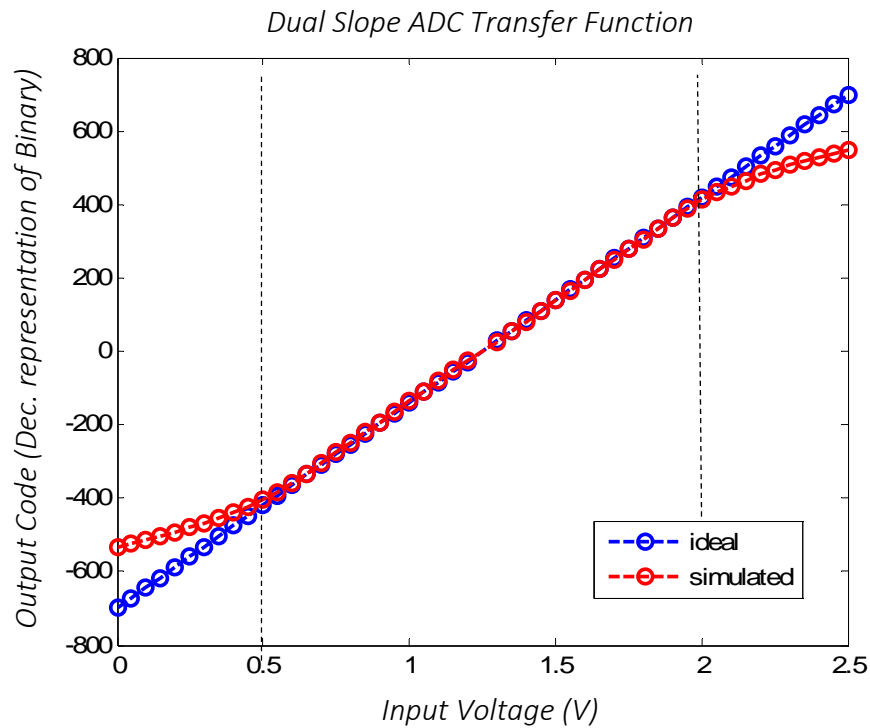
Figure 2.14: Simulated Transfer Function for Dual-Slope Integrating ADC

35

slope ADC are provided in Table 5. The ADC has an 11-bit signed digital output; this resolution was determined by the comparator delay and chosen RC values further discussed in Section 2.6.2.1. For simulation, a 10-bit counter was used with a 100MHz clock.

Table 5: Simulated Dual-Slope ADC Specifications

Specification	Value
Resolution	10-bits
Binary Representation	Signed
DC power consumption	5mW
Full Scale Range	0.5 – 2V
Offset Error	0 LSB
Gain Error	2 LSB

The current integrator is realized by connecting the opamp of Figure 2.7 in feedback with a capacitor and reset switch constructed from a standard transmission gate. The continuous time comparator is realized using a two-stage open loop amplifier follower by two inverting stages to bring the output rail-to-rail. The comparator operation and performance characterization is provided in Section 2.6.2.1.

2.6.2.1 Comparator

The designed continuous-time comparator implemented in the dual-slope ADC of Figure 2.13 is constructed from two open loop gain stages followed by a digital buffer seen in Figure 2.15. The final specifications for the designed comparator are provided in

Table 7. Monte Carlo simulations were used to estimate the comparator offset voltage of ~400uV. The results of the Monte Carlo simulation are provided

in Figure 2.16 below for 200 runs with a mean of 400uV and a standard deviation of 1.4mV.
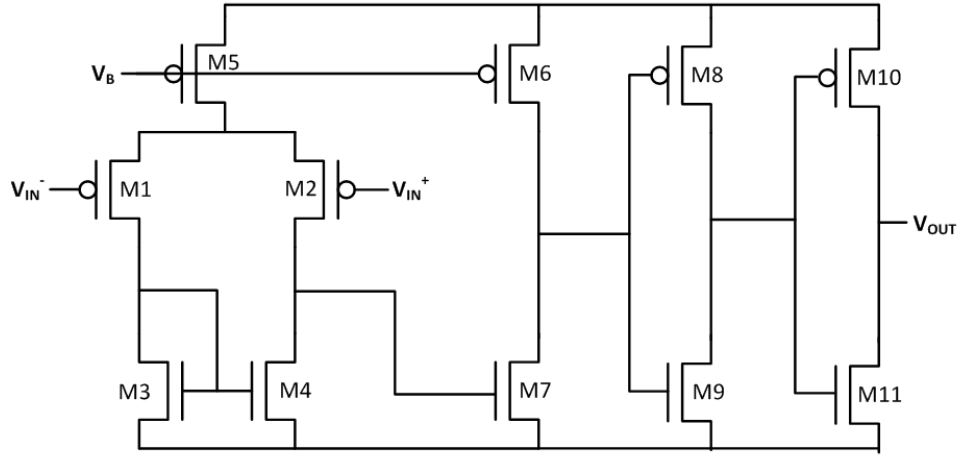
Figure 2.15: Continuous-time Comparator Design
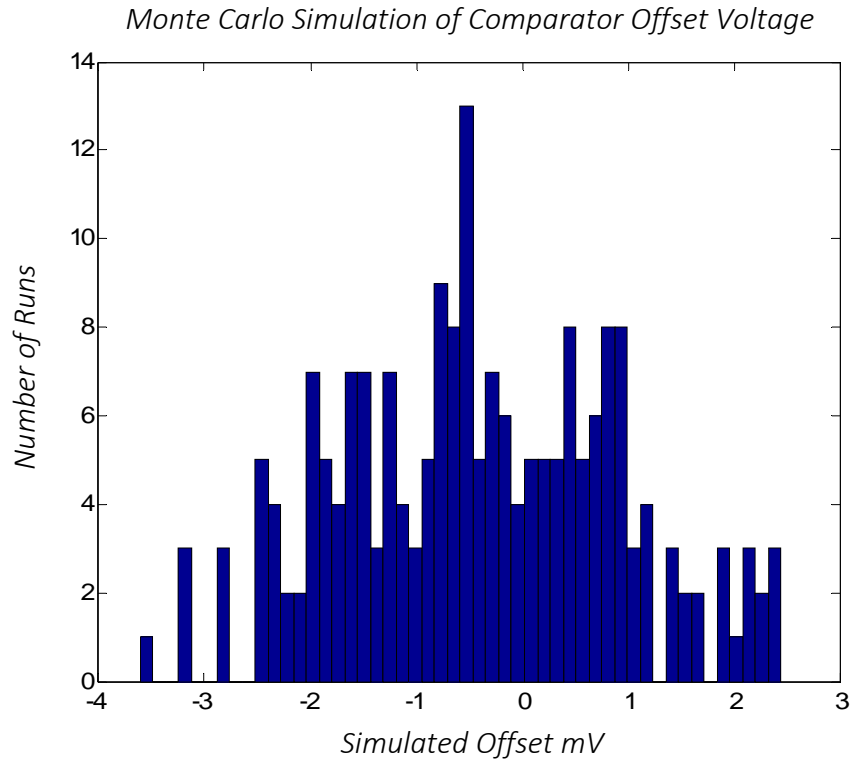
Figure 2.16: Monte Carlo Simulation for Comparator Offset Voltage

Table 6: Comparator Device Sizes

Device	Size	Device	Size
M1/M2	25/.32	M8	14/.32
M3/M4	14/3.2	M9	5/.32
M5	12.5/.32	M10	15.5/.32
M6	31/.32	M11	5/.32
M7	9/.32		

Within the scope of the dual slope ADC, the comparator functions as a zero-crossing detector where the input slope is always constant. Based on the chosen RC value, the inputs of the comparator will always see a slope of 347,222V/s determined by (9).

$$Input\ Slope = \frac{1.25}{RC} = \frac{1.25}{120K\Omega * 30pF} = 347{,}222\frac{V}{s} \qquad (9)$$

From Figure 2.17, one can find the associated delay to be roughly 5ns. The counter clock frequency (f_{CLK}) was thus chosen to be 200MHz. The maximum discharge time for a given cycle, T_{DIS_MAX}, is 2.9µs given by (10). Therefore the counter has a resulting 10 bit resolution determined by (11).

$$T_{CH\_MAX} = T_{DIS\_MAX} = \frac{RC}{1.25} = 2.9\mu s \qquad (10)$$

$$Bits = \log_2(T_{DIS\_MAX} * f_{CLK}) = 10\ bits \qquad (11)$$

Due to I/O constraints, only the top branch of the designed dual slope ADC was sent for fabrication. Due to an error in discharge voltage connection on the CMOS IC, the fabricated ADC requires a longer discharge time and thus has a lower bandwidth. Because of these issues, the ADC was not further characterized after fabrication due to its limited functionality and time constraints. The layout of the current integrator and comparator are indicated in Figure 2.18.
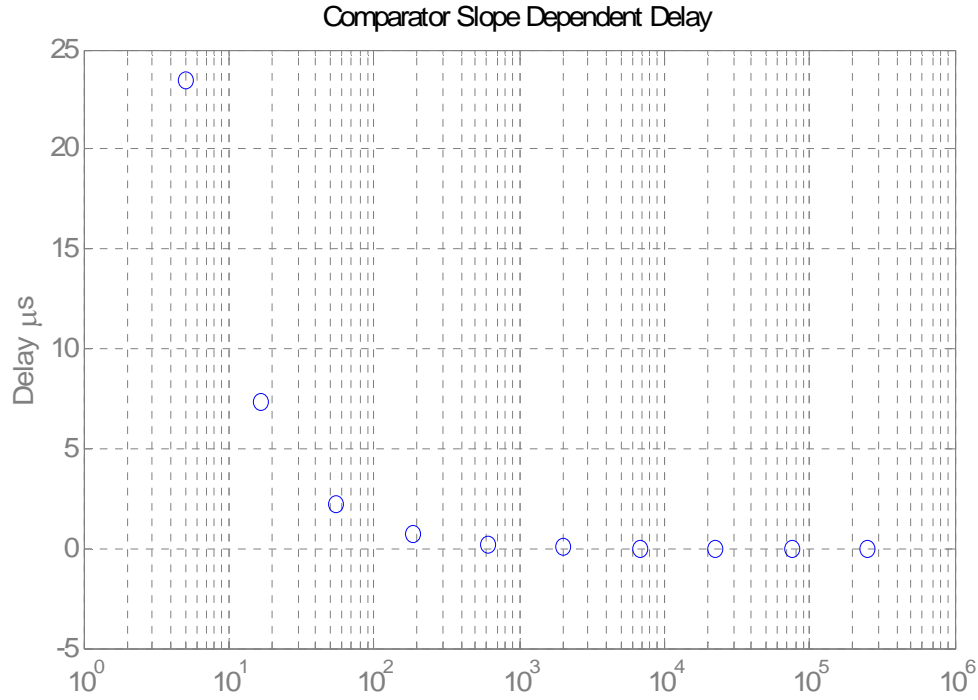
Figure 2.17: Input slope dependent comparator delay

Table 7: Key comparator specifications

Specification	Value
Static Power Consumption	630uA
Offset Voltage	4mV
Delay @ 10^5V/s	5ns
ICMR	300mV – 2.5V

39

2.7 CMOS IC Electrical Measurements

The class AB buffer amplifier was characterized with a 2V output voltage range and quiescent current of 1.32mA when operated with a 2.5V supply with a 10k load. The gain bandwidth product is measured to be 3.7MHz. The variable gain TIA has a dynamic range of 106dBΩ. While not fully optimized, these specifications are sufficient for sensing with the fabricated paper-based sensors. For reference, a comparison of the designed IC's electrical specifications compared to other published work from the past two years (2014-2015) is provided in Table 8. The final chip layout is provided in Figure 2.18.
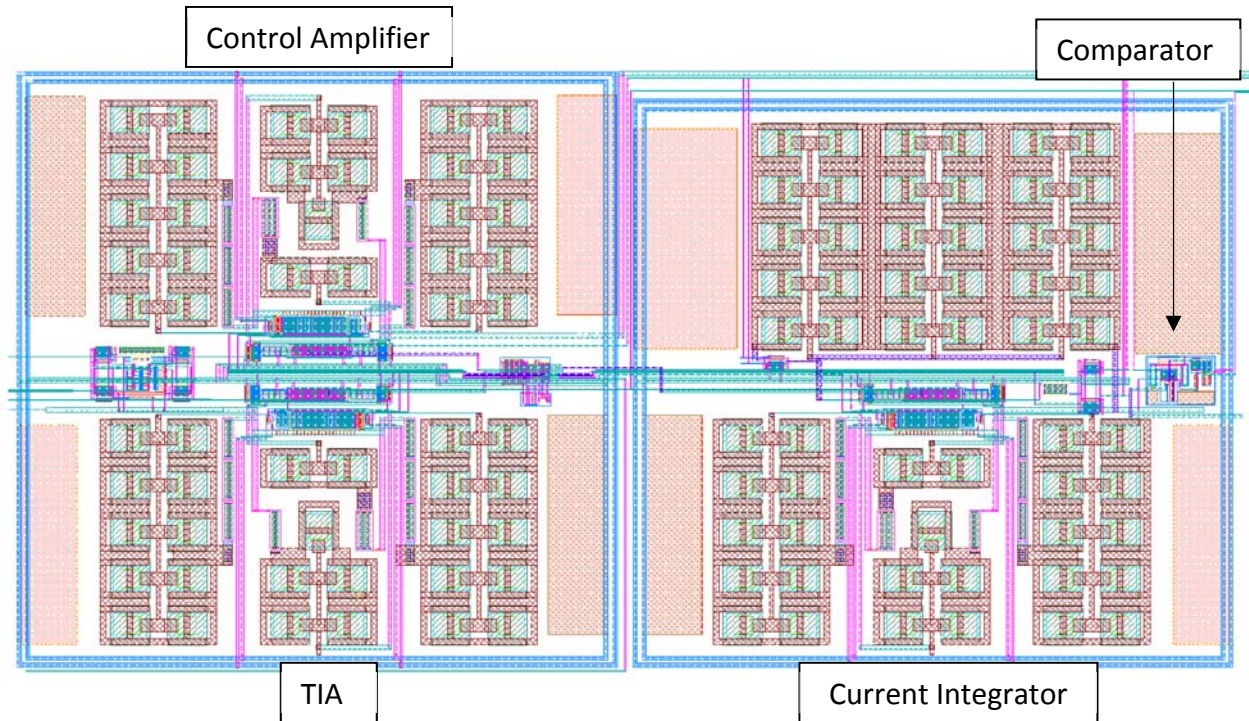
Figure 2.18: Complete CMOS Readout IC Layout

Table 8: CMOS Potentiostat Comparison to Recently Published Work

	This Work	[34] **(2013)**	[35] **(2014)**	[36] **(2015)**	[37] **(2014)**	[38] **(2014)**	[39] **(2010)**
Process	0.18μm	0.35μm	0.35μm	0.35μm	0.35μm	0.5μm	0.5μm
Supply	2.5V	3.3V	3.3V	1V	3.3V	5V	5V
Core Area	0.16mm^2	3.8x3.1mm	7.4x4.8mm	.13mm^2	2.04mm^2	1.5x3mm	340x150μm
Channels	1	192	64	1	1	6	1
Quiescent Power (per channel)	1.32mW	80μW	-	22μW	10mW	450μW[1]	11mW
RE Range (Output Swing)	2V	-	2.8V	-	-	rail-to-rail	-
Current Conv. Scheme	Resistive Feedback TIA	Current Conveyor	Direct Conversion (σ-Δ)	i-to-f	Current Conveyer	Resistive Feedback TIA	Resistive T Network TIA
Dynamic Range /dBΩ	106	80.35	140	31.36	126	-	120
Max Input Current	170uA	250nA	10μA	2.6μA	2.1mA	-	-
Input Referred Current Noise	7.5nA$_{RMS}$ [2] 0.82nA$_{RMS}$ [3]	-	540fA$_{RMS}$ [4] 250pA$_{RMS}$ [5]	-	-	-	1pA/√Hz [6]
Application	ePADs	Neuro-transmitters	-	Glucose Sensing	-	-	Heavy-metal ions
Meas. Scheme	3-elec	2-elec	3-elec	3-elec	3-elec	3-elec	3-elec

---

[1] 225μW per amplifier

[2] ±170uA input range

[3] ±1.9uA input range

[4] ±1nA input range, 2nd Order SD – 0-100Hz BW

[5] ±1μA input range, 2nd Order SD – 0-100Hz BW

[6] Noise density at 1kHz

3 Electrochemical Paper-based Sensors for Dopamine and Glucose Detection

The detection of dopamine, uric acid, ascorbic acid, glucose, lactose and pH measurement have been the focus of several paper based works because the presence of these molecules and their relative concentration are indicators of common and life threatening diseases such as kidney disease and diabetes which would readily benefit the developing world [40] [41] . Furthermore, all of these compounds can be detected with high sensitivity using electrochemical means [42, 43, 44]. The work presented in this chapter focuses on the development of amperometric and voltammetric ePADs for glucose and DA detection which can easily be extended for UA, AA and lactose. A potentiometric thread-based pH sensor was fabricated as part of a separate work and was tested for demonstration of potentiometric measurements using the designed potentiostat readout IC.

The first part of this chapter introduces mechanisms for amperometric and voltammetric sensing of glucose and dopamine and potentiometric pH measurement. Three ePADs were designed as part of this work and are subsequently described. The first ePAD is for single-analyte measurements and is termed a single-analyte ePAD. The second is a two-dimensional multi-analyte ePAD originally structured for multiplexed measurements of multiple analytes in one bulk solution with individual working and reference electrodes. The last is a 3-dimensional origami ePAD which aims to remedy the issues of the multi-analyte ePAD by using paper folding to create a 3D structure on top of the electroactive

area. The final section describes the fabrication of the thread-based potentiometric sensor for pH measurement.

3.1 Sensing Principles

3.1.1 Glucose detection principle

Commercial glucose sensors which use test strips such as the OneTouch UltraMini®, use chronoamperometry in conjunction with a catalyst, glucose oxidase, for electrochemical detection of glucose. Test strips consist of the typical 3 electrode test setup with a carbon counter electrode and Ag/AgCl reference electrode. The working electrode is doped with a mediator to aid electron transfer, often TMPD or potassium ferricyanide [45, 46].

In this electrochemical reaction, glucose is oxidized using glucose oxidase into gluconic acid. A concomitant reaction occurs at the working electrode which reduces Fe(III) to Fe(II) converting potassium ferrocyanide into potassium ferricyanide [16]. This reduction frees two electrons on the surface of the working electrode. These electrons migrate towards the working electrode, and thus the measured current at the working electrode is proportional to glucose concentration in the target analyte.

$$\text{Glucose} + 2K_3\left[Fe(CN)_6\right] + H_2O \xrightarrow{\text{glucose oxidase}} \text{Gluconic acid} + 2K_4\left[Fe(CN)_6\right]$$

$$2Fe(CN)_6^{4-} \xrightarrow{\text{anodic electrode}} 2Fe(CN)_6^{3-} + 2e^-$$

$$2Fe(CN)_6^{3-} + 2e^- \xrightarrow{\text{cathodic electrode}} 2Fe(CN)_6^{4-}$$

Figure 3.1: Glucose oxidation with glucose oxidase with potassium ferricyanide mediator [16]

3.1.2 Dopamine Detection

Cyclic voltammetry and amperometry are popular methods of dopamine detection [47]. Redox reactions involving dopamine are electrocatalytic; no mediator or enzymes are necessarily required for detection [48]. During electrochemical detection, dopamine is oxidized to dopamine-o-quinone and/or dopamine-o-quinone is reduced back to dopamine [49]. The resulting electrons from the half-cell reaction below are directly measured as a current.
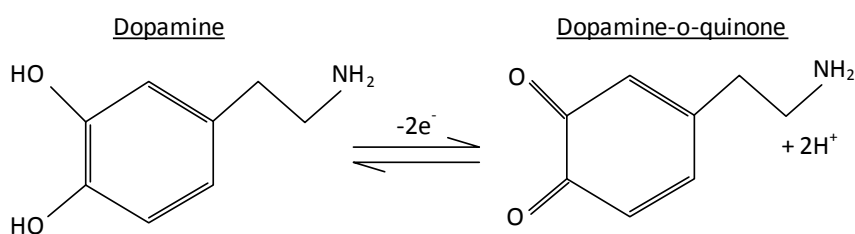
Figure 3.2: Dopamine/Dopamine-o-quinone half-cell reaction [49].

3.1.3 Potentiometric pH measurements with Polyaniline

Polyaniline in a polymer which (PANI) exists in three different oxidations states. One of these oxidation states, known as the emeraldine form, has a conductivity that is dependent on its degree of protonation. Thus, this form of polyaniline is

widely studied and used for its pH sensing capabilities. During protonation, hydrogen ions bond to empty nitrogen sites decreasing conductivity which decreases the open circuit potential. Since pH is a measure of hydrogen concentration, the open circuit potential will decrease with pH. PANI emeraldine base can produce an ideal response of (-60mV/pH) which has been demonstrated by numerous sources [50].
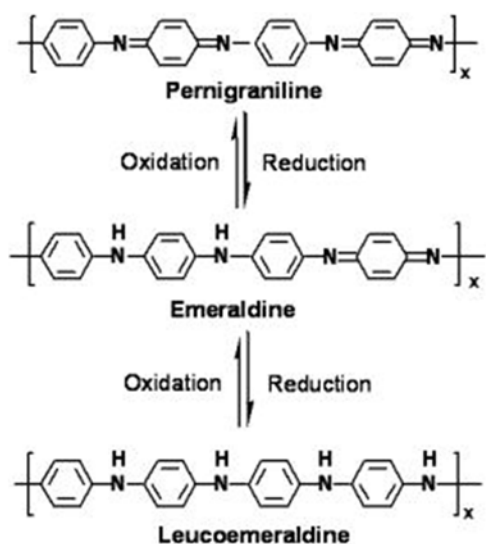
Figure 3.3: Polyanaline base reduction states [51]

3.2 Electrochemical Paper-based Analytical Device Design and Fabrication

3.2.1 Single analyte ePADs on Photo Paper

The single-analyte ePAD was fabricated on photo paper using the process outlined in Figure 3.4 for sensing of dopamine. Commonly available adhesive tape was patterned to create a mask through laser cutting (Versa, VLS2.40, power 40%, speed 20%) and affixed to photo paper (Epson S041913). The paper was then spin

45

coated with Ag/AgCl ink (Conductive Compounds, AGCL-675) and allowed to cure. The device was left in a desiccator for 30 minutes to remove any remaining residue. At this point three Ag/AgCl electrodes were formed. Carbon ink (Conductive Compounds, C-200 Carbon Resistive Ink) was subsequently screen printed on two of these electrodes and the patterned tape was peeled off leaving an Ag/AgCl RE, a carbon CE and a carbon WE. Dielectric ink was then painted on top of the device to protect all of non-sensing areas and pads from contact with the aqueous bulk solution. To aid in painting of the dielectric ink, a plastic mask was patterned with the laser cutter and attached to the paper device using an aerosol spray. The plastic mask was subsequently removed. An optical image of the resulting paper based device along with an SEM of the screen printed ink is provided in Figure 3.5.
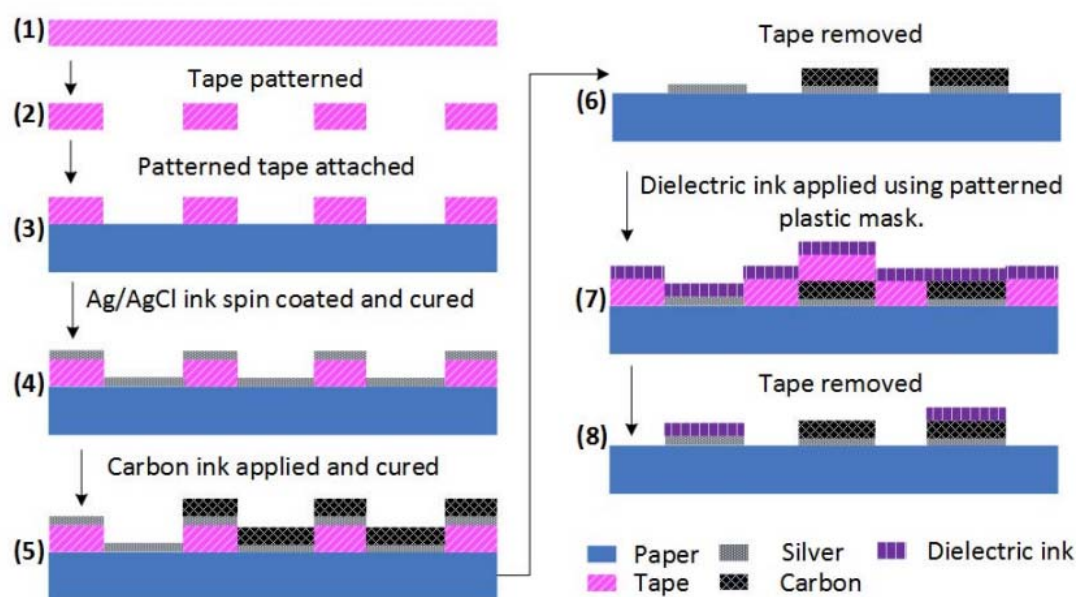
Figure 3.4: Single-analyte ePAD fabrication process

46

Because the sensor was fabricated for DA sensing, the carbon WE was left bare. One advantage of this device is that the substrate is completely hydrophobic so no analyte is absorbed into the sensor. Therefore the sensor can theoretically be used for multiple measurements after rinsing in between.

The results of sensing with these sensors is provided in Section 4.2. While promising, there were several issues with this ePAD which motivated a redesign of the sensors. Primarily, the sensors had no structure for holding analyte and thus required an additional piece of equipment for use, either a flow cell or a beaker. Furthermore, these sensors were only capable of single analyte measurements.
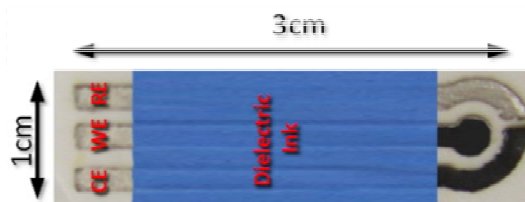
Figure 3.5: Fabricated single-analyte ePAD

3.2.2 Multi-analyte ePADs

To remove the need for a flow cell and expand the ePAD for sensing of multiple analytes, the multi-analyte ePAD shown in Figure 3.6 was designed. This design uses fluidic channels created through wax printing of a hydrophilic substrates to wick the bulk solution to four sensing zones, each capable of sensing a different analyte. Solution is dropped in the center of the ePAD; 15-20ul of analyte is appropriate to saturate the hydrophilic regions for sensing. In this design, the electrochemical reaction occurs at the interface of the paper and screen printed electrode unlike the previously described single-analyte ePAD where the reaction

occurs on the top surface. Because bulk solution is contained to the hydrophilic areas, no dielectric ink is needed to protect the non-sensing areas of the screen printed electrodes.

Fabrication of multi-analyte ePADs was completed using the modified process outlined in Figure 3.7. In short, Whatman® Grade 1 chromatography paper wax printed on both sides (Xerox ColorQube 8580). Paper was heated at 140°C for 10 minutes to allow wax to penetrate through paper leaving four hydrophilic zones and a fluidic channel integrated within the paper. Separately, vellum adhesive (Chartpak DAF8) was patterned using a laser cutter (Versa, VLS2.40, power 40%, speed 20%)) to create a mask for screen printing of electrodes. The pattern mask is

Figure 3.6: Multi-analyte ePAD

Figure 3.7: Multi-analyte ePAD fabrication process
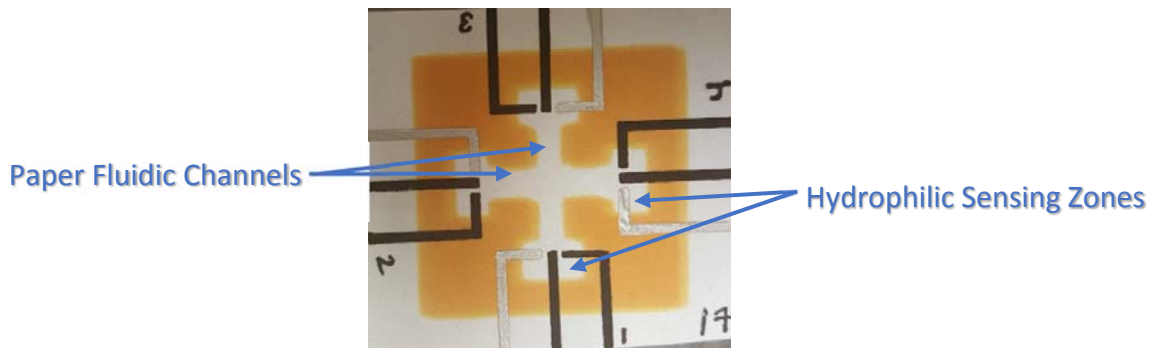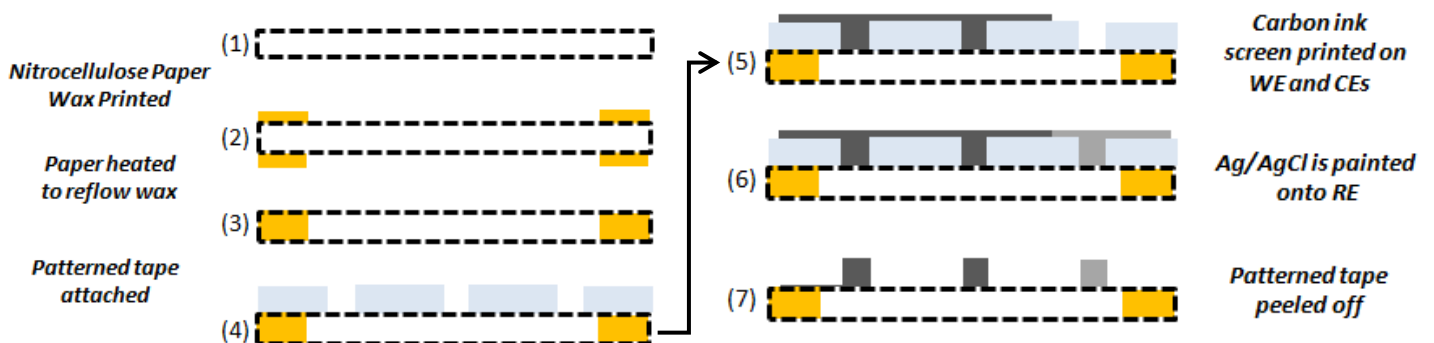
aligned to channels and Ag/AgCl ink is painted onto the RE and Carbon ink is painted onto the WE and CEs yielding the sensor seen in Figure 3.6.

The Whatman® Grade 1 chromatography paper on which the sensors are fabricated is popularly used for paper-based sensor fabrication [6, 52]. The chromatography paper is created from a network of woven cellulose fiber and is very non-uniform as confirmed by the surface profiles provided in Figure 4.8. This leads to variations in sensor output as a result of surface area variations further discussed in Section 4.2. To help mitigate the variations in the multi-analyte device, a modified ePAD structure was fabricated which contains a 3D structure to both contain bulk solution and prevent its contact with non-sensing areas.

3.2.3 3D Origami ePAD

Inspired by previously designed hollow channel PADs, a 3-dimensional ePAD structure was designed to mitigate the variation in electrodes seen with the multi-analyte ePAD. Two primary changes were made to the previous ePAD design; 1) the design was changed so that the electrochemical reaction occurs on the top surface of the screen printed electrode where there is more control over the final electrode planarity and 2) a 3D structure realized using simple paper folds was created to confine the volume on top of the electrode to a fixed amount and protect the non-sensing areas of the electrode from contact with the bulk solution. To accommodate these changes, a completely hydrophobic surface was needed to screen print electrodes.

Wax printing of the chromatography paper and subsequent diffusion through the paper left a hydrophobic substrate on top of which electrodes can be screen printed. While any hydrophobic paper substrate could have been used, this substrate was advantageous as the resulting paper was thin enough to fold several times, not true of other hydrophobic substrates such as the Epson® photo paper, but was still firm enough to transport without bending when picked up as with wax coated parchment paper. A profile of the screen printed carbon electrodes compared to the paper surface is provided in Figure 4.8. There is an 8.4µm standard deviation in surface profile on the bare chromatography paper compared to just 1.3µm on the surface of the screen printed electrodes. Thus, the active area of the screen printed electrodes on the 3D ePAD device have a more uniform active area than the previously described multi-analyte ePADs.

The resulting 3D paper based sensors were fabricated using the following procedure. Whatman® grade 1 chromatography paper is wax printed with the device pattern using a standard printer (Xerox ColorQube 8580). The paper is heated on a hotplate at 100°C for 3 minutes or baked at 150°C for 5 minutes to allow wax to flow through the paper. Devices are manually separated and double-sided tape is adhered to the specified areas. The device is folded in an accordion fashion as shown in

Figure 3.8 and the appropriate area is laser cut (Epilog Zing 24, power 25%, speed 80%) leaving a cavity in the device which will become the sample reservoir.
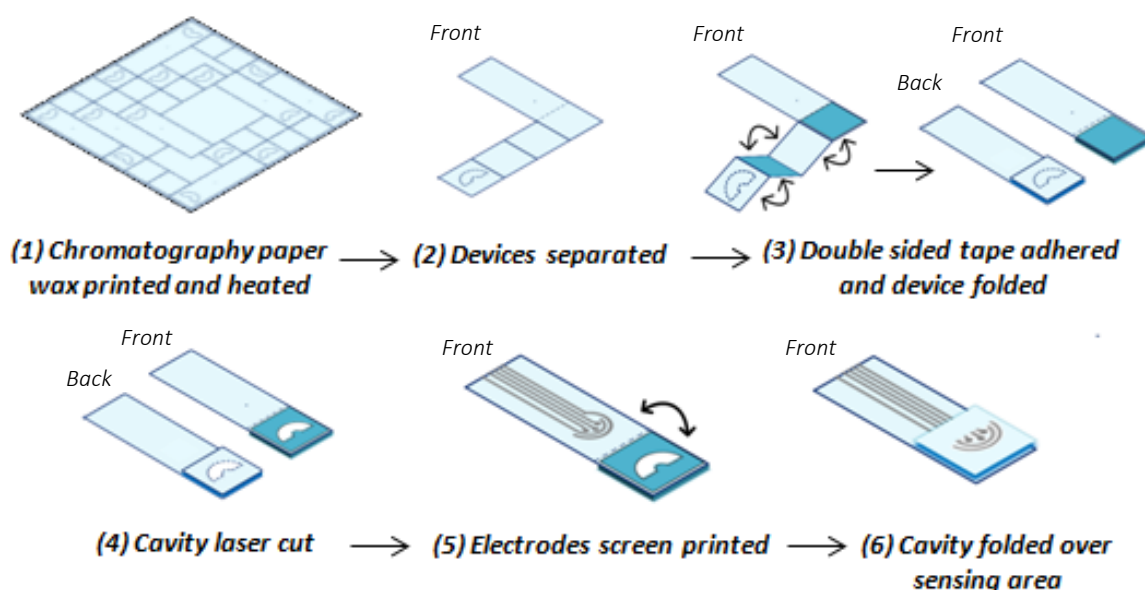
Figure 3.8: Folding procedure for 3D ePAD

The electrochemical sensors are subsequently screen printed onto the nitrocellulose paper using the process outlined in Fig. 3. Briefly, standard adhesive tape is patterned using a laser cutter (Epilog Zing 24, speed 100%, power 8%). The patterned tape is adhered to the nitrocellulose paper using an alignment marker on the device pattern. Ag/AgCl ink is screen printed onto the RE and cured by heating at 70C. Carbon ink or a carbon ink mixture containing 50mM potassium ferricyanide is then screen printed onto the WEs and CEs. The required biomediators, such as glucose oxidase, are then drop cast onto the WEs. The tape is removed leaving an Ag/AgCl RE, a carbon CE and three WEs. The double-sided tape on the inside of the cavity is peeled and the cavity is folded over to isolate the sensing area and create a reservoir for the sample yielding the final structure. The reservoir is capable of holding 300ul of analyte.

Electrodes were designed to for equal distance between all working electrodes with respect to the reference electrode and counter electrodes. Working electrodes have a 1mm radii and 1mm from the counter electrode in the smallest dimension. The RE is radially 2mm from the counter electrode.
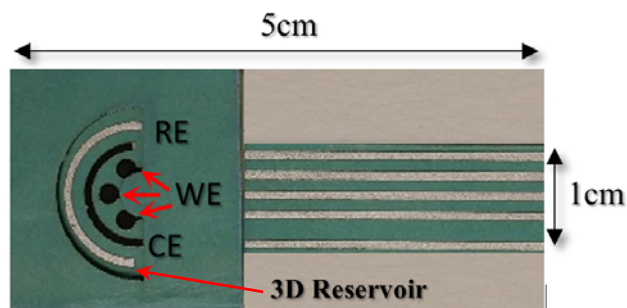

Figure 3.9: Resulting 3D ePAD containing a reservoir for bulk solution. 3D structure is realized by a combination of paper folding and laser cutting in conjunction with double-sided tape
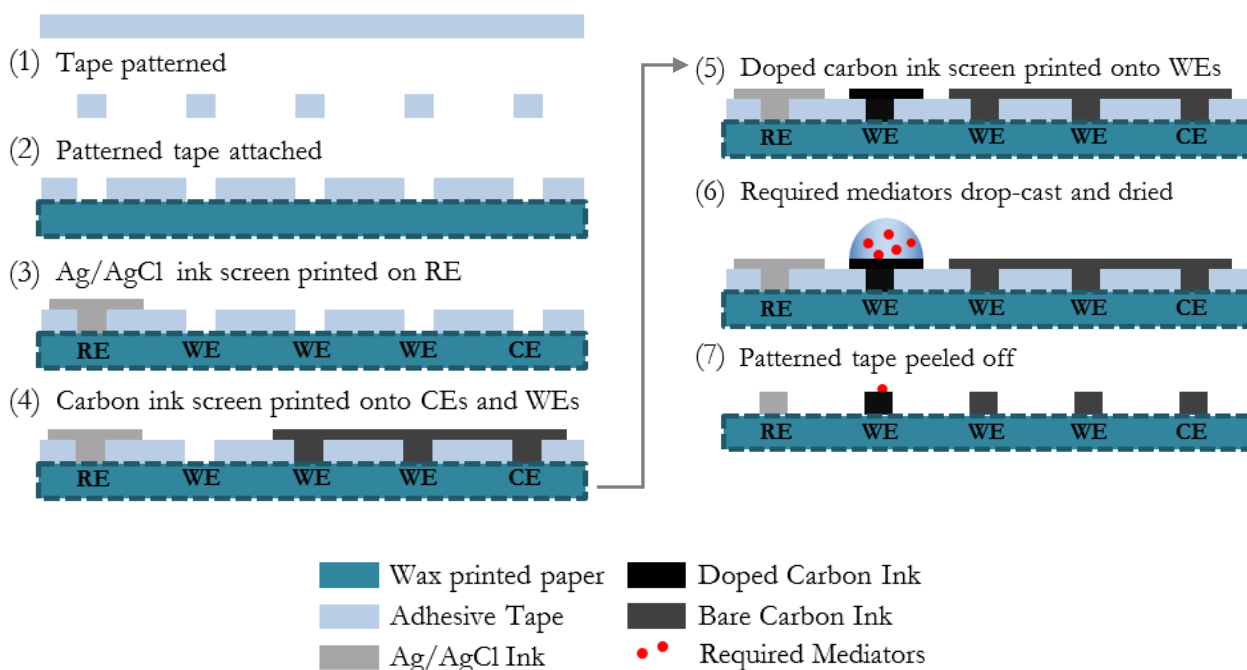
Figure 3.10: 3D ePAD fabrication process

3.2.4 Thread-based pH Sensor

Paper-substrates are a popular substrate for ASSURED devices due to their low-cost, accessibility and easy disposal by incineration. An easy extension of paper-substrates is thread, which takes the 2D paper based sensors to the third dimension while maintaining the properties of paper that make it so useful for low cost diagnostic applications [53].
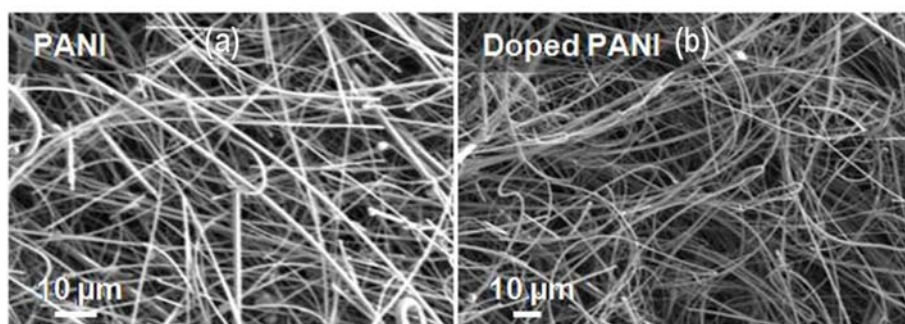
Figure 3.11: SEM image of PANI before (left) and after (left) doping with HCl [54].

A thread-based potentiometric pH sensor was fabricated as part of a separate work with polyaniline emeraldine base using the following procedure. Briefly, 500mg of PANI (Figure 3.11) was doped with 20ml of 0.1M HCl from Sigma Aldrich. The two were stirred in a -4 degree C ice bath for 5 hours. The resulting ink was used in a specialized coating setup described in Figure 3.12. Thread is dipped in ink using a pulley system to uniformly coat thread and is subsequently dried using a heat gun. Resulting thread is recollected on a second spool. The resulting thread was kept in a dessicator before usage [54].
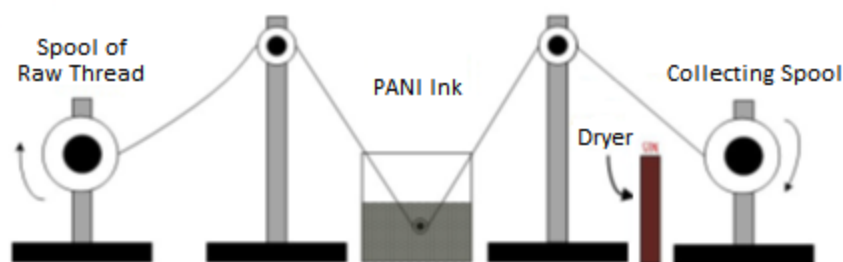
Figure 3.12: Thread coating procedure. Thread is dipped in ink using a pulley system to uniformly coat thread and is subsequently dried using a heat gun. Resulting thread is recollected on a second spool. Adapted from **[54]**.

4 Results and Discussion

This chapter provides the results of sensing with the fabricated ePADs and designed potentiostat. The first section of this chapter demonstrates that the designed potentiostat is capable of electrochemical measurements with potassium ferricyanide tests using commercial electrodes. Voltammetric and amperometric testing results with the single-analyte ePAD, multi-analyte ePAD and 3D origami ePAD are subsequently provided. The single analyte ePAD is demonstrated for dopamine detection using both CV and chronoamperometry. The problems of the 2D ePAD are illustrated with potassium ferricyanide tests and the 3D ePAD is demonstrated for dopamine and glucose detection using cyclic voltammetry and chronoamperometry. Measurements are taken using both a commercial potentiostat (CHI760E) to validate ePAD functionality as well as with the designed potentiostat demonstrating the complete sensing device. Potentiometric sensing results with the thread-based pH sensor follow this. The chapter concludes with a discussion of work yet to be completed.

4.1 Verification of potentiostat functionality with KFe$_3$(CN)$_6$

To demonstrate the electrochemical sensing capabilities of the potentiostat readout IC described in Chapter 0, commercial electrodes were used for sensing of potassium ferricyanide. Potassium ferricyanide is commonly used as a mediator in electrochemical measurements and is standard for electrochemical measurement and calibration and was thus used [55, 26]. An external Ag/AgCl RE, a platinum CE and a gold WE were used in addition to LT317A voltage regulators, a Keithley 6221 DC/AC Current Source, a Rigol DS1102E oscilloscope and a Tektronix AFG3102 function generator for testing. A simple lowpass FIR filter with a 1Hz cuttoff frequency was used for processing of the data in MATLAB. For initial verification of the designed potentiostat function, a standard 6mM potassium ferricyanide in phosphate-buffered saline (PBS) solution was tested using cyclic voltammetry with the commercial gold WE. The test setup is seen in Figure 4.1.

One key result demonstrated the potentiostat readout ICs use for electrochemical measurements: in the right panel of Figure 4.2, peak current increases linearly with the square root of scan rate, as predicted by the Randles-Sevcik equation (3) with an r-squared value of 0.9894. One such cyclic voltammagram from which this data is taken is shown in the left panel of Figure 4.2.
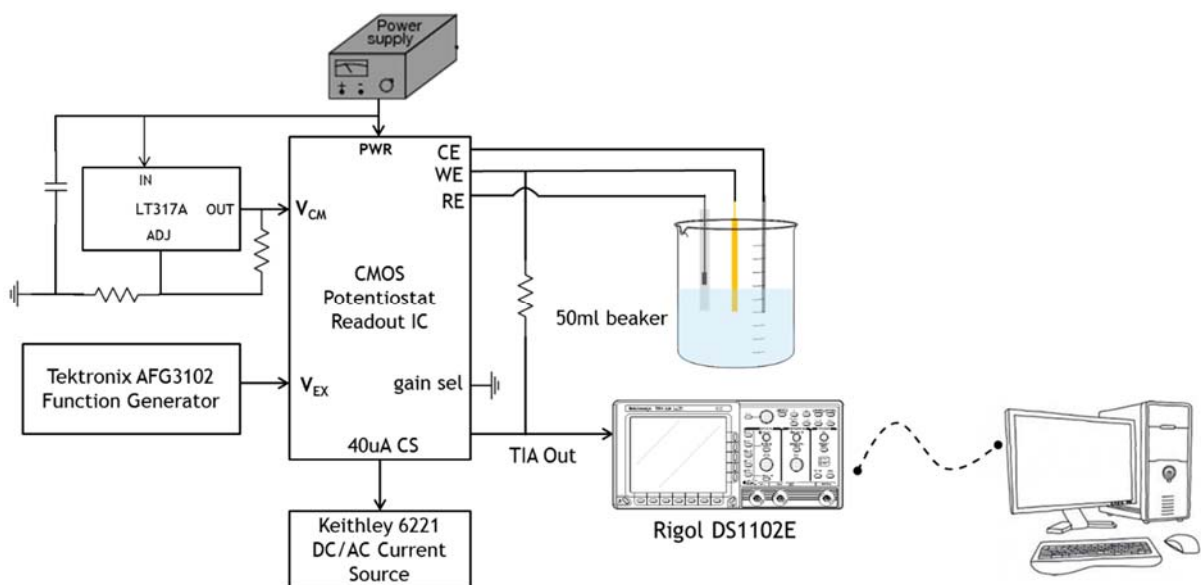
Figure 4.1: CMOS Potentiostat Readout IC Test Setup. Data is acquired using a Rigol DS1102E oscilloscope and is transferred to a PC for processing.
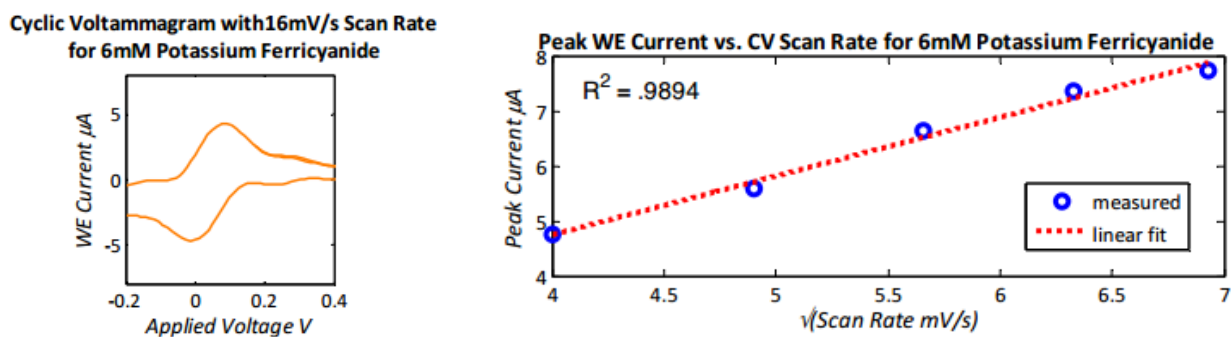
Figure 4.2: Cyclic voltammagram (left) and peak WE current vs CV scan rate for commercial electrodes with 6mM KFe$_3$(CN)$_6$

4.2 Single-analyte ePAD for Dopamine Sensing

Two measurement methods were used with the single-analyte ePAD for detection of dopamine, CV and chronoamperometry. For measurements, a Pt CE and commercial reference electrode were used with the paper-based carbon WE described in Section 3.2.1. Experiments were performed by immersing all three electrodes in ~30ml of solution in a 50mL beaker and using the same data acquisition protocol described in Section 4.1. A fixed distance was kept between

56

the WE and CE using a ring stand and a milled piece of aluminum designed to fit over the top of the beaker with openings for the CE, WE and RE.

For CV measurements, a 100mV/s input ramp from -1 to 1V was applied for a full cycle, shown in Figure 4.3. One resulting cyclic voltammagram is seen in the top panel of Figure 4.4. The peak cathodic current was plotted against dopamine concentration for individual tests using a single sensor which indicated a linear relationship in peak output current with dopamine concentration as predicted by the Randles-Sevcik relationship. Sensitivity was 1 mA/mM-cm^2 using this method.

For chronoamperometry, a fixed 5V potential was applied and the equilibrium current was plotted against dopamine concentration as seen in the bottom panel of Figure 4.4 which again resulted in a linear relationship as predicted by the Cottrell equation as expected. The sensor exhibited a sensitivity of 851μA/mM-cm^2 using this method. Slightly lower than the sensitivity obtained using CV.
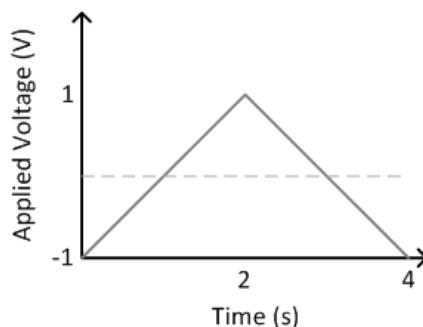
Figure 4.3: Applied CV excitation waveform for dopamine sensing with the fabricated ePAD.
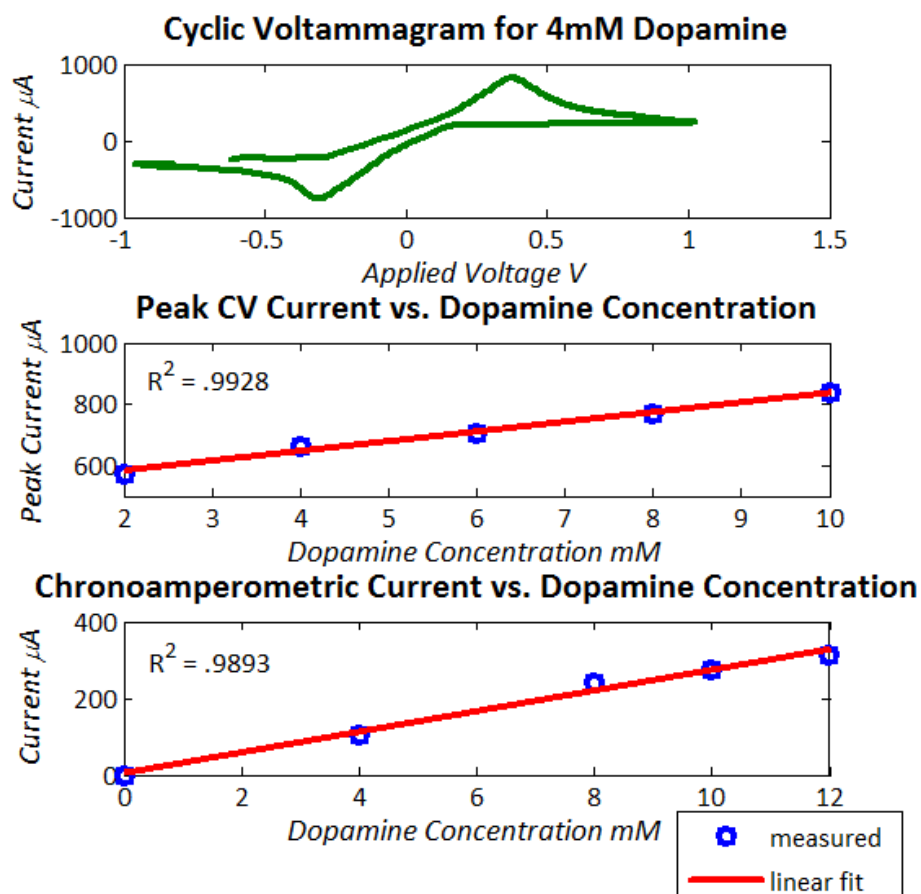
Figure 4.4: Cyclic Voltammagram (top) and Peak Current vs. DA Concentration for fabricated ePAD using cyclic voltammetry (middle, Vapp = 100mV/s) and chronoamperometry (bottom, 5V fixed).

4.3 Characterization of the multi-analyte ePAD

The multi-analyte ePAD was fabricated for dopamine sensing which resulted in inconsistent results. Unlike the single-analyte ePAD which could be rinsed between uses for multiple measurements, the multi-analyte ePAD uses the paper substrate on which it is fabricated to wick the bulk solution to the various sensing zones on the substrate therefore every measurement requires use of a new sensor. It was thus important that the multi-analyte ePADs were fabricated consistently

such that the variations in the base current due to the mediator reacting with the bulk solution do not overshadow changes in current due to analyte concentration.

To ascertain the quality of the screen printed electrodes for sensing, 25 sensing zones on 13 multi-analyte ePADs were tested using CV with 15mM $KFe_3(CN)_6$. A CV excitation waveform of with a 100mV/s ramp from -0.4 to 1V was applied to obtain a cyclic voltammagram for each sensor. A histogram of the peak cathodic current for these sensors is provided in Figure 4.5. A subset of the cyclic voltammagrams from which the histogram is obtained is provided in Figure 4.6. For 25 sensors, there is a 3.3uA standard deviation (σ) in current from the mean

Cyclic Voltammagrams for 15mM $KFe_3(CN)_6$ in PBS

Maximum Peak Cathodic Current for 25 Bare Sensing Zones

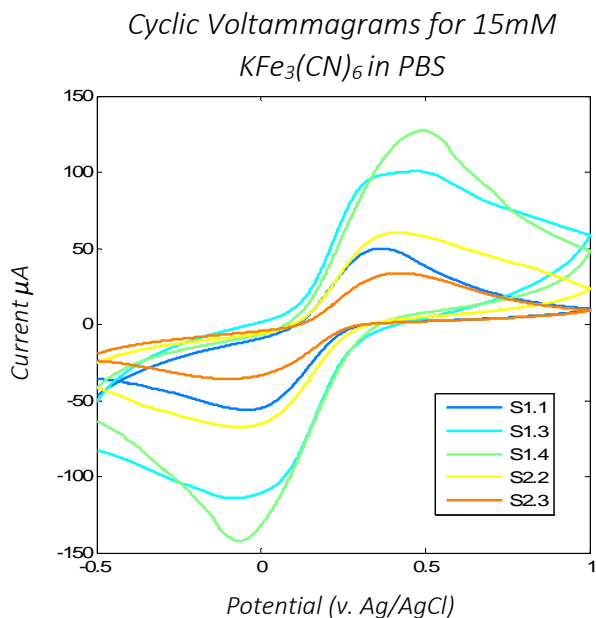**Figure 4.6: Cyclic Voltammagrams for screen printed sensor with 15mM $KFe_3(CN)_6$**
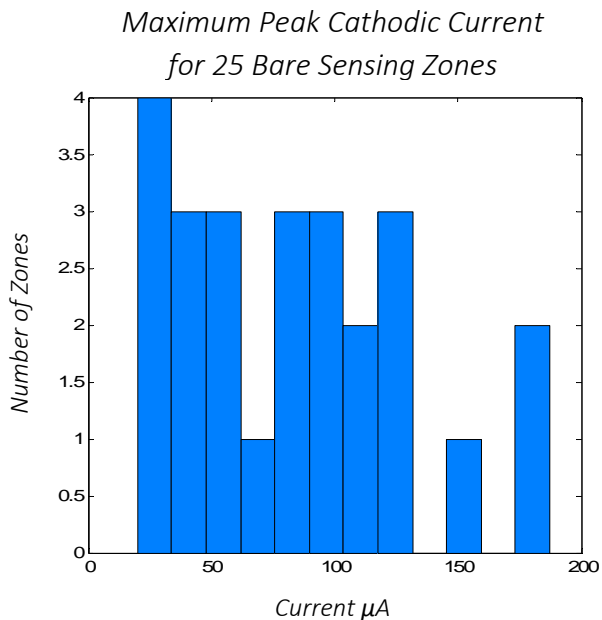
Figure 4.5: Histogram of peak cathodic current for 25 sensing zones

value of 50.7uA. Ideally, 2σ would be less than 1-2% of the average current value as the variation will set the detection limits of the sensor when functionalized.

To better understand the source of these peak current deviations, 3D variations in the sensors electroactive area were assessed. SEM and standard optical images of sensors' screen printed carbon ink and the wax printed substrate were
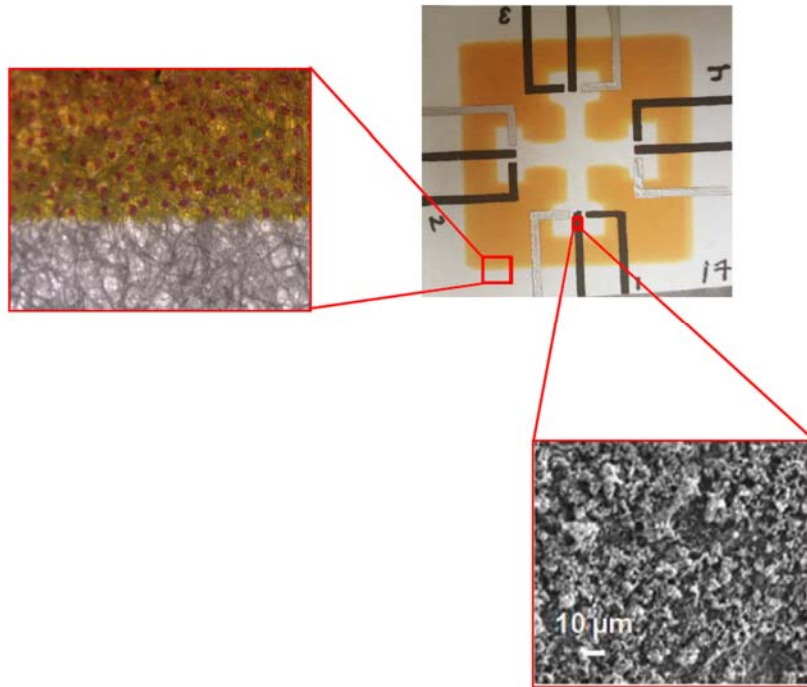
Figure 4.7: Carbon Electrode SEM Image [53]

examined and are provided in Figure 4.7. As is evident from these images, there is non-uniformity in both the paper substrate and the top surface of the printed ink which is confirmed by the surface profiles taken using a DektakXT contact profilometer. The resulting profiles, seen in Figure 4.8, show a 8.4μm standard deviation in surface area on the bare Whatman® grade 1 chromatography paper and 1.32μm standard deviation on the top surface of a screen printed carbon electrode.

The bottom surface of the screen printed carbon electrodes can be assumed to have a profile that is the exact inverse of the bare chromatography paper.

Since the electrochemical reaction in these devices occurs at the interface of the electrode and paper, the variation in the surface profile of the substrate will contribute to variations in the electroactive area of the WE. Due to this variability in fabrication, the sensor was not implemented for sensing, instead focus was place on improvement of the sensor design for more consistent fabrication and reliable measurements, resulting in the 3D origami ePAD of Section 3.2.3.
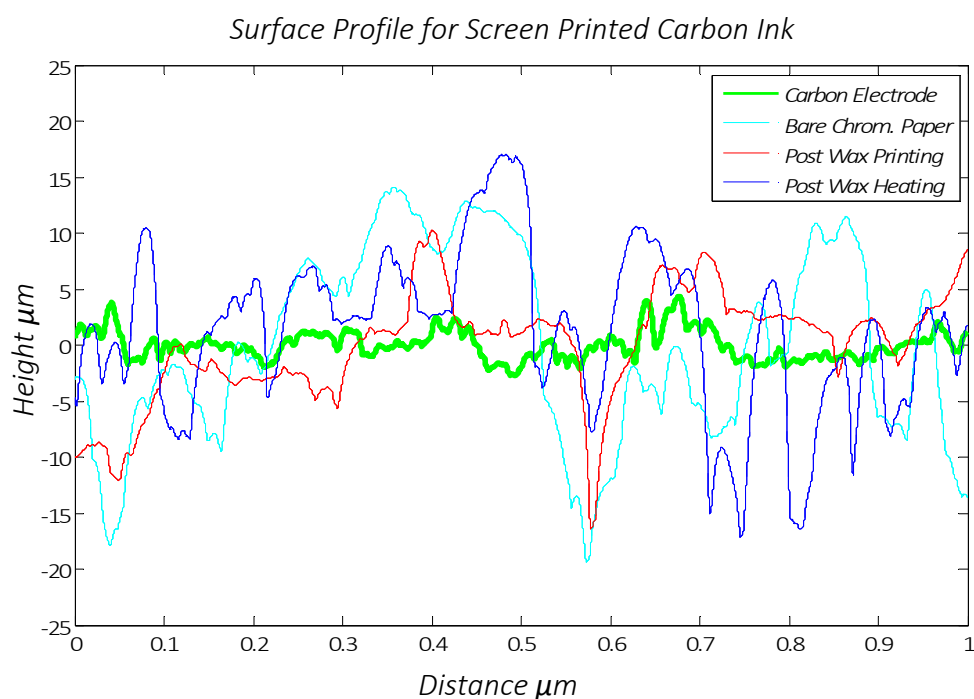
Figure 4.8: Surface profile for screen printed electrode substrate and ink

4.4 3D Origami ePAD for Dopamine and Glucose Sensing

4.4.1 Data Acquisition

To streamline data acquisition with the 3D origami ePAD (3D ePAD) using the CMOS potentiostat readout IC, board level electronics were implemented around the readout IC to provide power and the appropriate bias voltages. The board was designed for interface with a National Instruments DAQ and subsequent data acquisition and processing in a LabVIEW® graphical user interface. A block diagram illustrating the boards operation is provided in Figure 4.9.
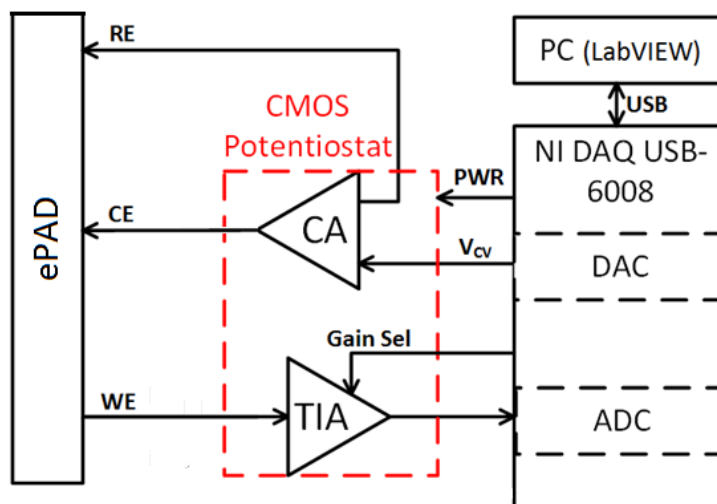
Figure 4.9: Data Acquisition Configuration

COTS IC's were implemented around the CMOS potentiostat readout IC to realize the appropriate bias currents using a Texas Instruments REF200 current source. An optical image of the final board is shown in Figure 4.11. The final board layout is provided in Appendix D: Potentiostat Board Layout.

A LabVIEW interface was developed to interface with the potentiostat and board level electronics. The simple interface was created using an NI DAQ USB-

6008. The DAQ was used to supply power to the fabricated CMOS IC as well as digitize the output of the variable gain TIA. The graphical user interface allows for control of all CV parameters and the transimpedance gain and applies a simple low-pass FIR filter (25 taps, 30Hz cutoff) to acquired data. Am image illustrating the interface design is provided in Figure 4.10.
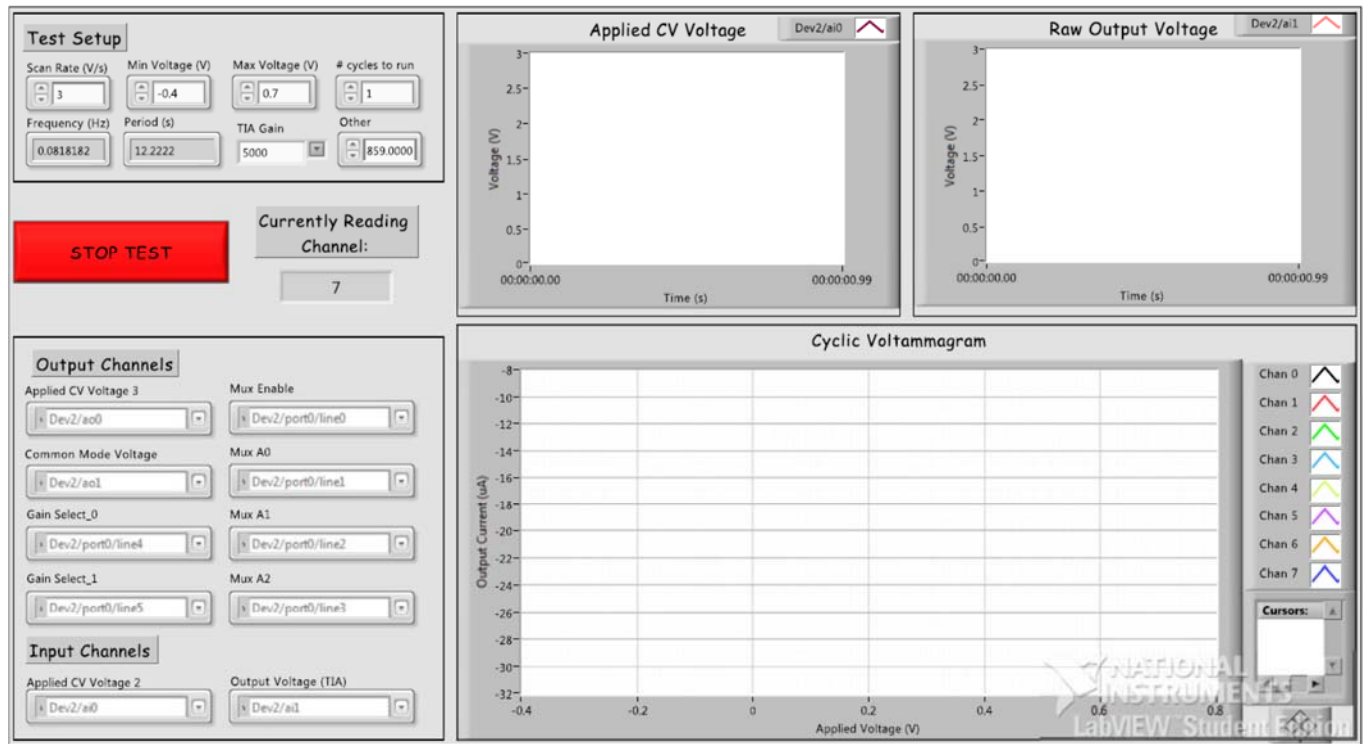
Figure 4.10: LabVIEW® based Graphical User Interface for Potentiostat Parameter Selection
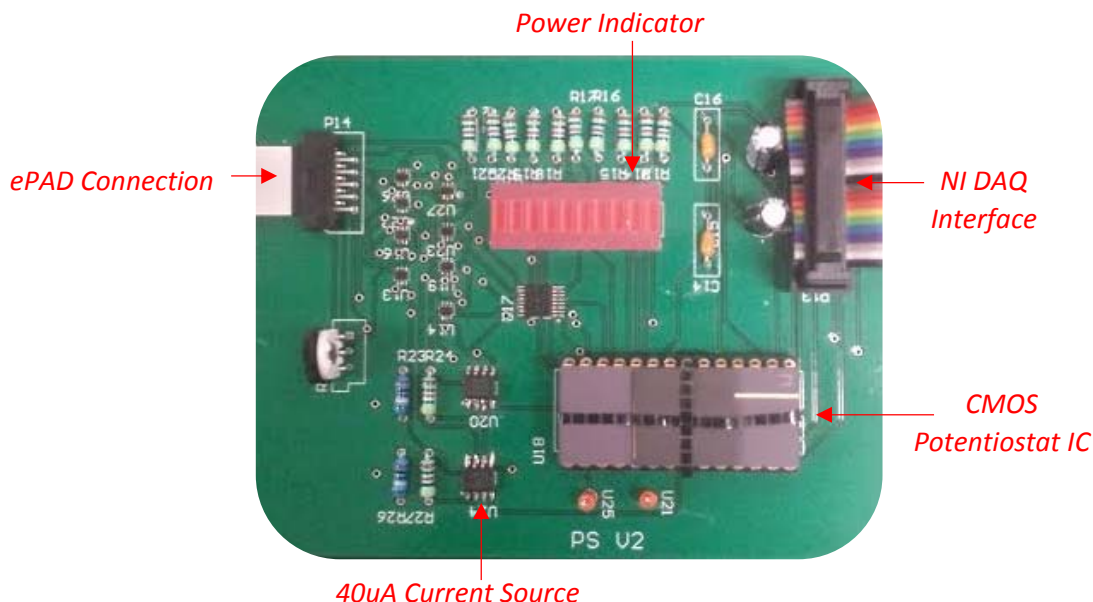
Figure 4.11: CMOS Potentiostat PCB with board level components for data acquisition

4.4.2 Comparison to Commercial Potentiostat

As a preliminary test, 3D ePAD measurements were compared for DA detection using a commercial bench-top Potentiostat (CH Instruments, Model 760E) and the data acquisition setup described in Section 4.4.1. With four folded layers, the paper-based reservoir is capable of holding 300uL of sample, thus 300uL aliquots of 5mM and 10mM DA in PBS were sequentially pipetted into the reservoir and CV was employed to ensure peak cathodic and anodic currents occurred at the appropriate potentials and the extent of reversibility of the system. The input signal was ramped from -0.8V to 0.8V at 120mV/s for a full cycle to obtain the cyclic voltammagrams in the bottom panel of Figure 4.12. This process was repeated after connecting the

sensor to the CMOS potentiostat via the onboard flexible cable connector resulting in the cyclic voltammagrams seen in the top panel of Figure 4.12.

Both sets of curves demonstrate an increase in peak anodic and cathodic current with concentration and contain oxidation and reduction peaks at roughly 0.5V and -0.3V as expected for bare carbon electrodes used for dopamine detection [56]. The difference in current magnitudes for the two sets of CVs can be explained by variability in the electrode fabrication process.
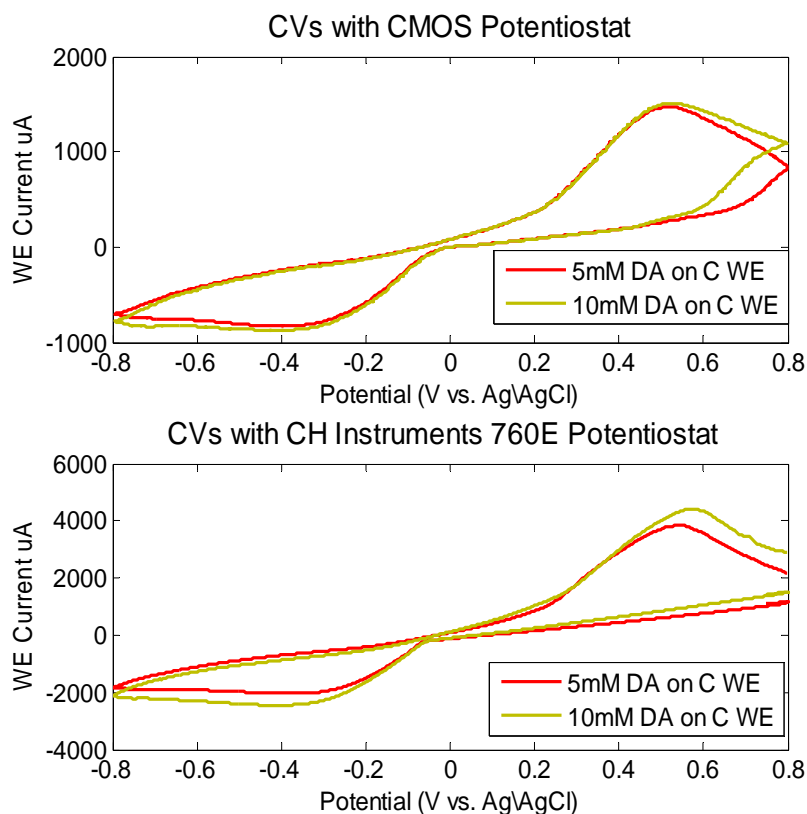
Figure 4.12: Comparison of Commercial Potentiostat to CMOS IC for varying DA concentration

4.4.3 Low-level Dopamine Detection

For determination of the electrochemical PADs sensitivity to dopamine, four DA concentrations between 0.01mM and 0.3mM in PBS were sensed using CV employed by the CMOS potentiostat system. All measurements were taken without the use of bench-top equipment. The input signal was again ramped from -0.8V to 0.8V at 120mV/s resulting in the CVs seen in Figure 4.13.

The key result is a linear increase in anodic current with DA concentration with an R^2 value >0.9 as theoretically expected [13]. The resulting linear fit has a slope of 284uA/mM for the 1mm radius WEs translating to a sensitivity of $\approx$9mA/mM-cm^2.
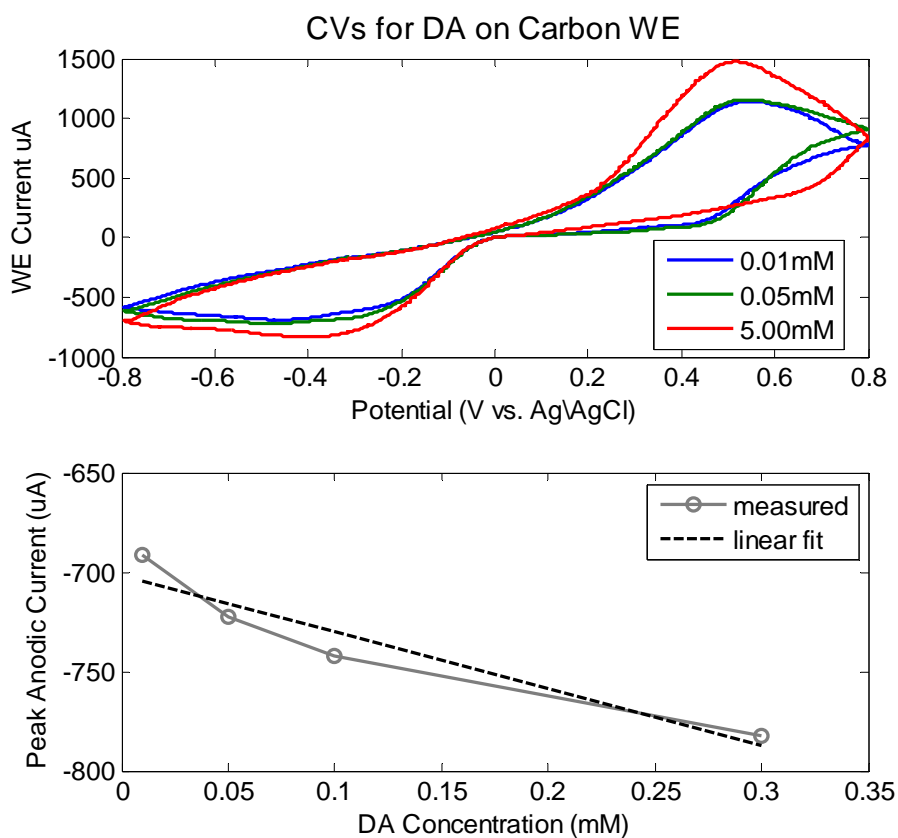
Figure 4.13: Low concentration dopamine detection with 3D ePAD

4.5 α-D-Glucose Detection with the 3-Dimensional ePAD

PADs were functionalized for α-D-glucose detection through drop casting 3uL of 5mg/mL glucose oxidase (Sigma Aldrich, Type VII, >100u/g) on the screen printed WEs doped with potassium ferricyanide. To ensure the glucose oxidase was present on the electrodes, the functionalized devices were subject to a bulk solution containing 20mM glucose in PBS using a commercial potentiostat. The obtained CV curves seen in Figure 4.14 exhibited peaks at the expected 500mV oxidation potential demonstrating the functionalize PADs sensitivity to glucose [57]. The shift in peak location occurs with scan rate due to the transition from reversible to irreversible electrochemical reactions with increasing scan rate.
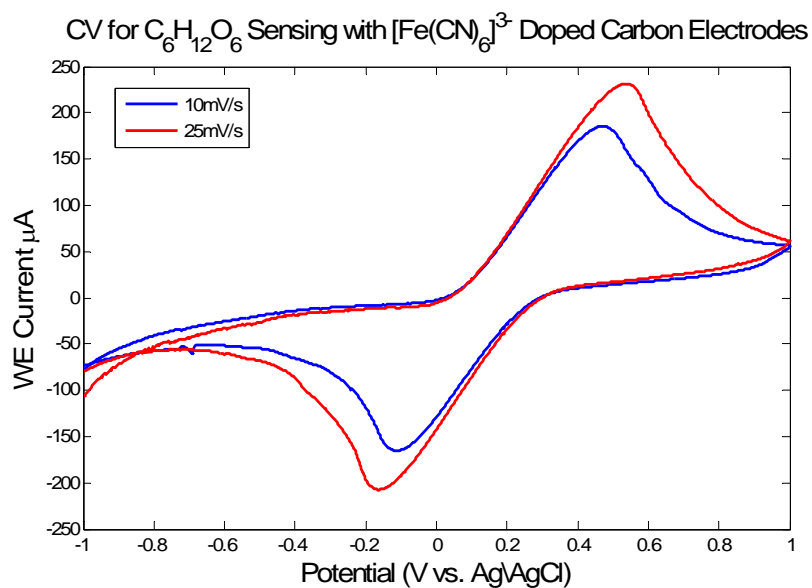
Figure 4.14: Cyclic Voltammagrams with increasing scan rate for 20mM Glucose detection

To determine the sensors sensitivity to glucose, all electrodes on the 3D origami ePADs were functionlized with glucose oxidase and were tested with increasing glucose concentrations using the CHI760E commercial potentiostat. Three measurements were collected from each ePAD, one from each WE. Figure 4.15 shows the resulting chronoamperograms with the obtained calibration curve in the bottom panel. The data shown is the average of valid data sets for a given measurement. In some cases only one measurement was valid due to connection issues. As theoretically expected by the Cotrell equation, there is a linear increase
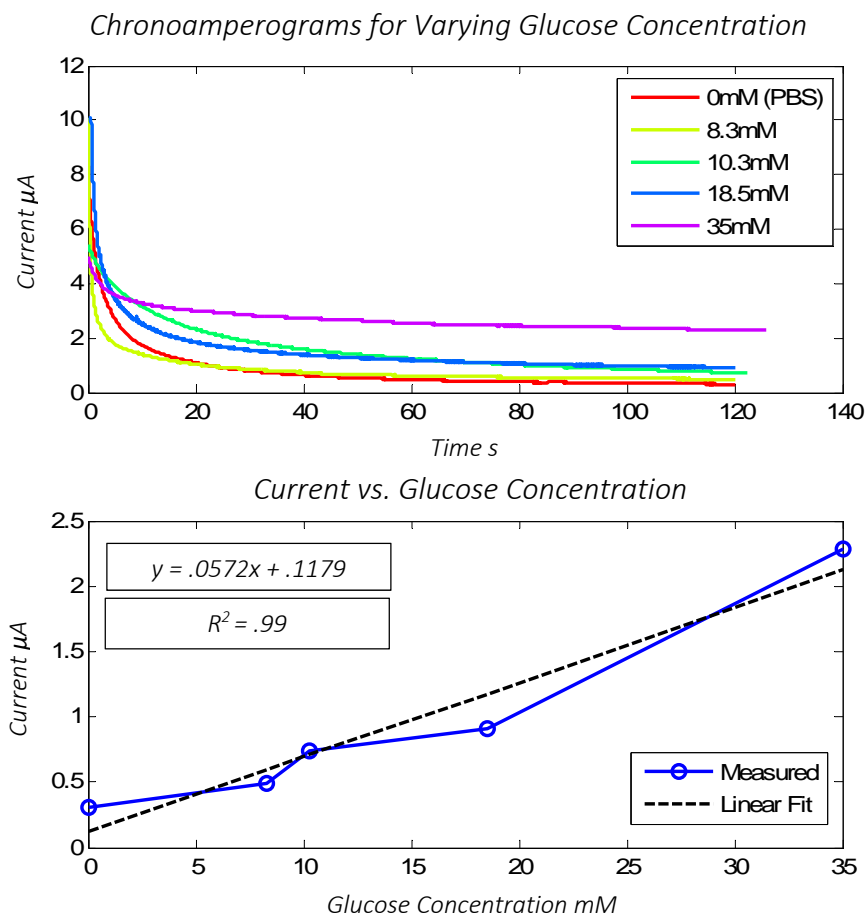
Figure 4.15: Chronoamperograms (top) and current at 120th second vs. α-D-glucose concentration for glucose sensing with the 3D ePAD. Average of three measurements are shown. In some cases only one measurement was deemed valid due to connection issues.

in equilibrium current with α-D-glucose concentration. The 57.2nA/mM slope gives the sensor a resulting sensitivity of 1.82uA/mM-cm^2 when using chronoamperometric measurements.

4.1   pH Measurement with Polyaniline

To demonstrate full functionality of the potentiostat readout IC, the potentiostat board was reconfigured as seen in Figure 4.16 for potentiometric measurements using the previously described thread based pH sensor.
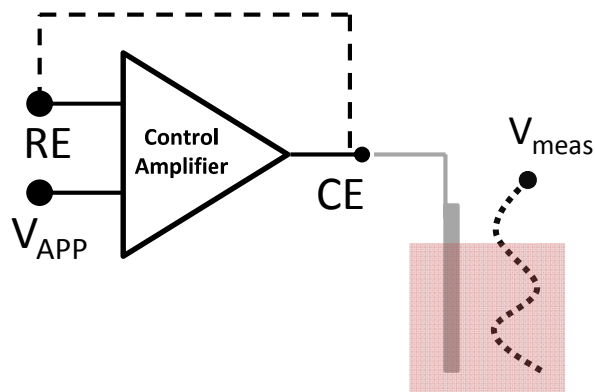
Figure 4.16: Class AB Amplifier Configuration for Potentiometry

For testing, thread was submersed in standard pH buffer solutions and the open circuit voltage was measured using a NI DAQ and LabVIEW interface as previously described (Section 4.4.1). As seen in Figure 4.17, the resulting data shows a linear increase in open circuit voltage (v. Ag/AgCl) as theoretically expected by the Nernst equation. The slope of the best fit line for the acquired data gives the thread-based pH sensor a sensitivity of 54mV/pH, close to the theoretical detection limit of 60mV/pH [53].
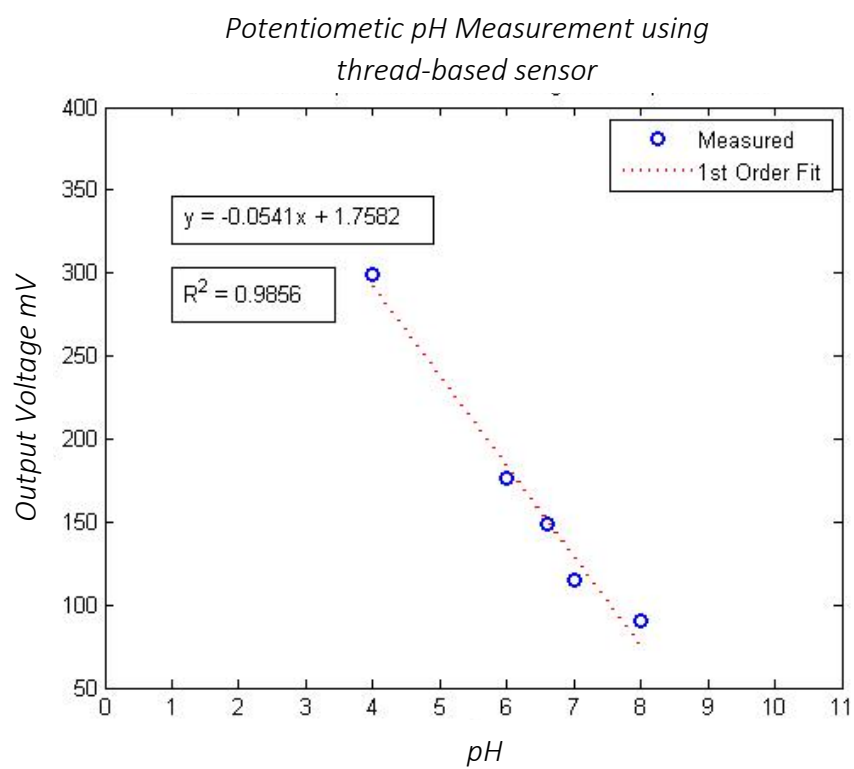
**Figure 4.17: Potentiometric pH Measurements taken with PANI coated
thread-based sensor**

5 Conclusions and Future Work

This thesis contributes three electrochemical paper-based sensor designs and a custom CMOS potentiostat readout IC which together work towards a multi-analyte low-cost diagnostics platform. The core of the CMOS potentiostat readout IC is a class AB amplifier which realizes a control amplifier and TIA. The IC was electrically verified and implemented at the board level for a system that is capable of taking 8 multiplexed measurements.

Three ePAD designs were fabricated and demonstrated with the readout IC for sensing of dopamine and α-D-glucose on various substrates. The final 3D ePAD uses paper-folding to create a reservoir for containment of bulk solution and protection of non-sensing areas during measurement. Additionally, the designed class AB amplifier was demonstrated to be viable for potentiometric measurements through testing with a thread-based pH sensor. While promising, there is still a significant amount of testing to be done.

Thorough interference studies are yet to be completed for both dopamine and glucose detection. Most critically, numerous sources have shown that ascorbic acid (AA) interferes with electrochemical dopamine detection which is of concern as both substances are present in human blood [48]. Several works and have developed techniques for increasing specificity which included addition of special membranes which aim to separate the redox voltages of AA and DA [48, 58]. Similarly, α-D-glucose sensitivity when sensing in mixed in solutions containing other glucose forms, lactose, fructose and other sugars is yet to be completed. Only after

interference studies are complete can integration of WEs for multiple analytes on a single ePAD occur.

Additionally, reference electrode stability is yet to be evaluated. RE stability relies on the ability of the Ag/AgCl electrode to react with the bulk solution to maintain its potential. When the AgCl has reacted completely the RE is no longer functional. Studies investigating the duration of RE stability are pertinent when multiple measurements are to be taken.

Other immediate work includes exploration of alternate electrochemical techniques for detection. Differential-pulse voltammetry is one technique of interest which may aid to remove the variations in current due to electrode area by allowing time for decay of the nonfaradic current [59]. If other techniques are to be evaluated, the designed Class AB amplifier on the CMOS potentiostat readout IC should be improved in future iterations.

While the amplifier had adequate performance for the application on hand, the amplifier will not have the required bandwidth for use with techniques such as fast-scan cyclic voltammetry which requires application of excitation signals of 1MV/s. Bandwidth of the amplifier can be extended in this application without sacrificing power through reduction of the unnecessarily high DC gain. Additionally, while better than buffers with no adaptive loads, the quiescent current variation with process is still high for the designed amplifier. In portable applications, power consumption will be limited placing importance on this parameter. The variation seen may be attributed to the mismatch in threshold voltages of the p and n-type input devices of the class AB buffer portion of the

opamp. Migration back to the original topology presented in [31] may result in less

variation due to this reason.

Appendix A: Class AB Amplifier Simulation

The designed class AB amplifier was fabricated in the IMB180 process through MOSIS fabrication service. Measurement of the various operational amplifier parameters are described below.

DC gain:

Measurement of amplifier DC gain was completed using the amplifier in the closed loop configuration seen in Figure A.1 below and connecting a capacitive load at the output.
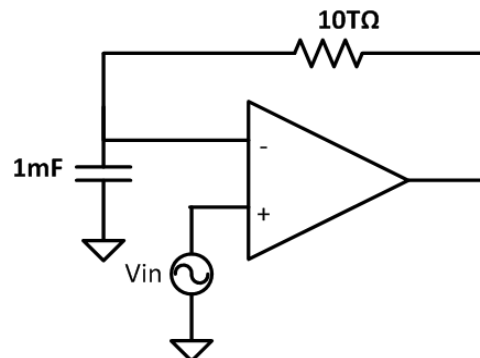
Figure A.1: Class AB Configuration for Measurement of DC Gain. The amplifier is open at frequencies >15uHz

Use of this configuration allows for easy measurement of DC without concern for differences in threshold voltage at the input of the class AB portion of the opamp which cause the output to saturate. At DC, the capacitor connected to the inverting input is open which operationally leaves the amplifier in unity gain configuration. At frequencies greater than 1/RC, the impedance of C becomes small, essentially shorting to ground effectively rendering the amplifier open-loop. The simulated DC gain is provided in Figure A.2 below and was simulated to be ~145dB.
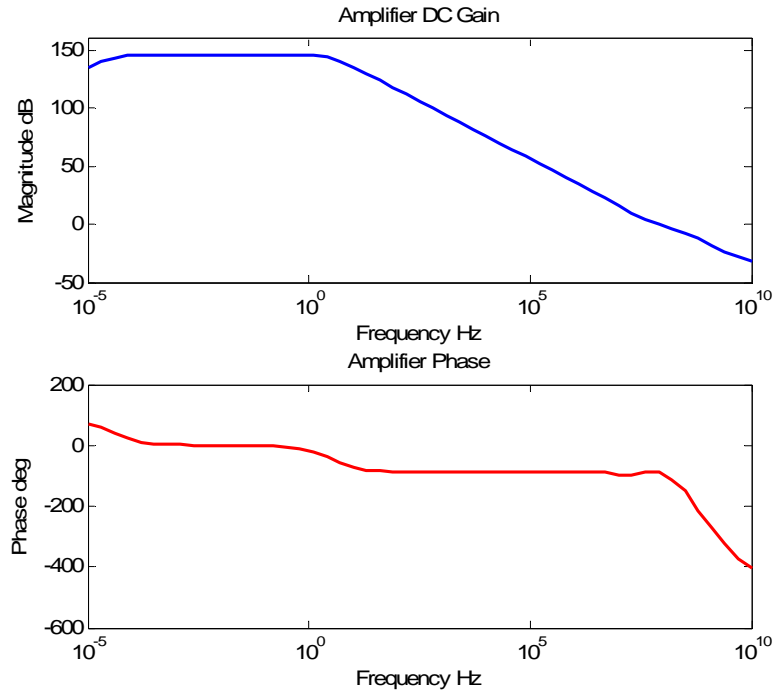
Figure A.2: Simulated DC Gain for Class AB Amplifier

As is true of all Class AB amplifiers, the biasing point will change with the addition of a resistive load changing the DC gain of the amplifier. For resistive loads greater than 10Ω, the class AB amplifier's DC grain remains above 73dB. A plot of the DC gain vs. the resistive load is provided in Figure A.3.

75
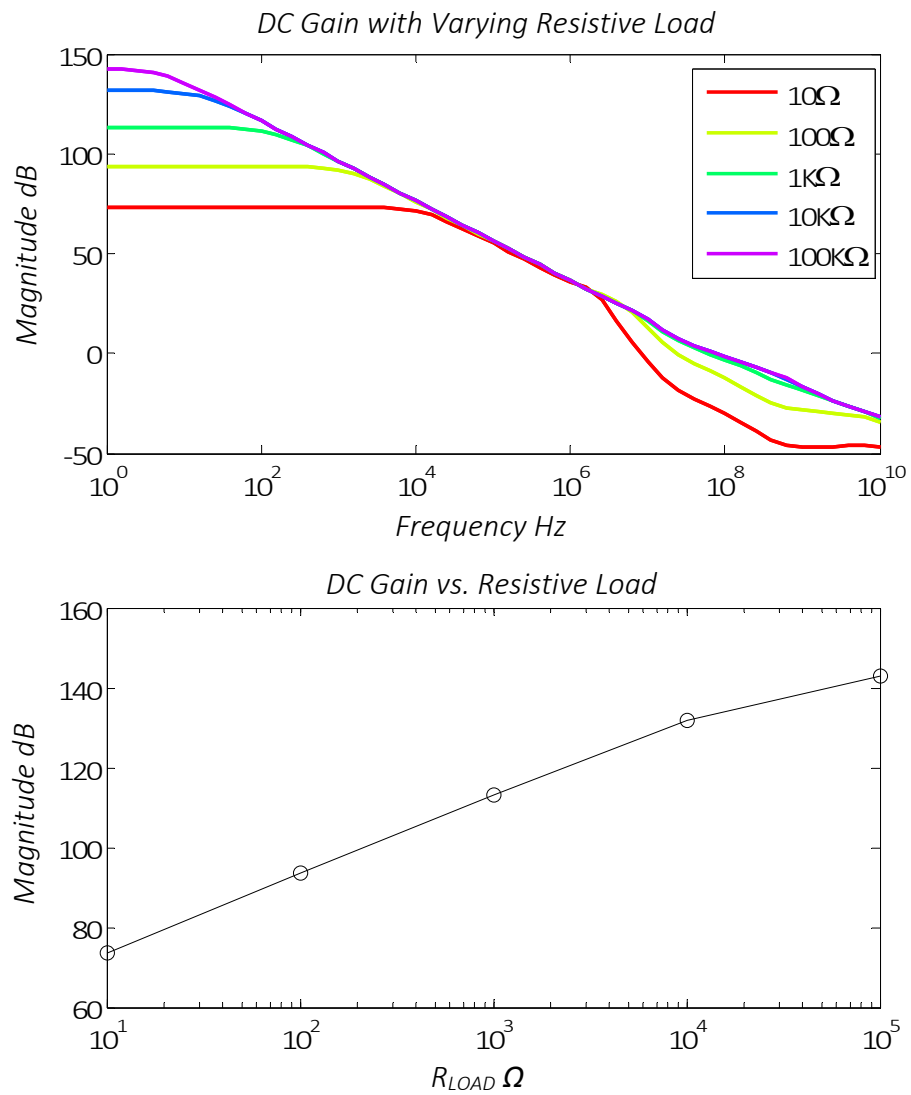
Figure A.3: DC gain with varying resistive load for Class AB Amplifier

Rejection Ratios:

The common-mode rejection ratio is defined as the amplifiers differential gain divided by the common mode gain. For measurement of the common-mode gain, the amplifier was configured as seen in Figure A.4 below.
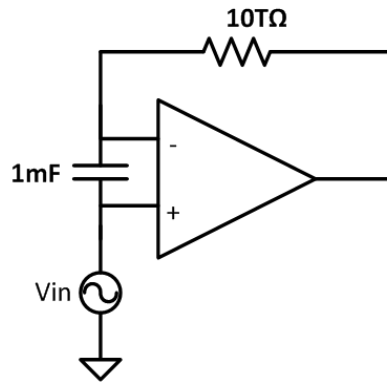
Figure A.4: Class AB Amplifier Configuration for CMRR

This configuration functions in a very similar way to that used for DC gain measurement. At frequencies above 1/RC the impedance of the capacitor becomes small shorting the amplifier inputs together. The simulated CMRR is provided in Figure A.6 and was determined to be ~330dB in the bandwidth of the amplifier.

The power supply rejection ratio is defined as the ratio of the differential gain to the power supply gain. To determine the power supply gain the configuration seen in Figure A.5 was used. Again the configuration functions in a similar manner to that previously described to maintain the DC operation point of the amplifier

without concern for differences in threshold voltage and offset voltage. The PSRR

is approximately -60dB in the bandwidth of the amplifier.
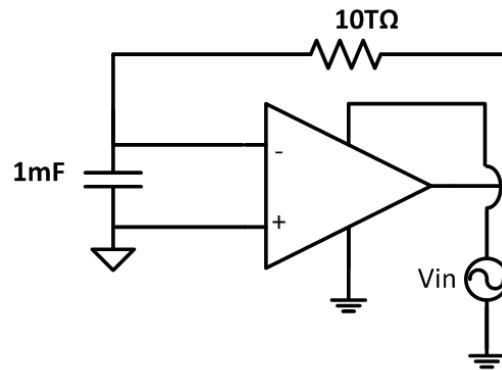
Figure A.5: Simulation configuration for PSRR
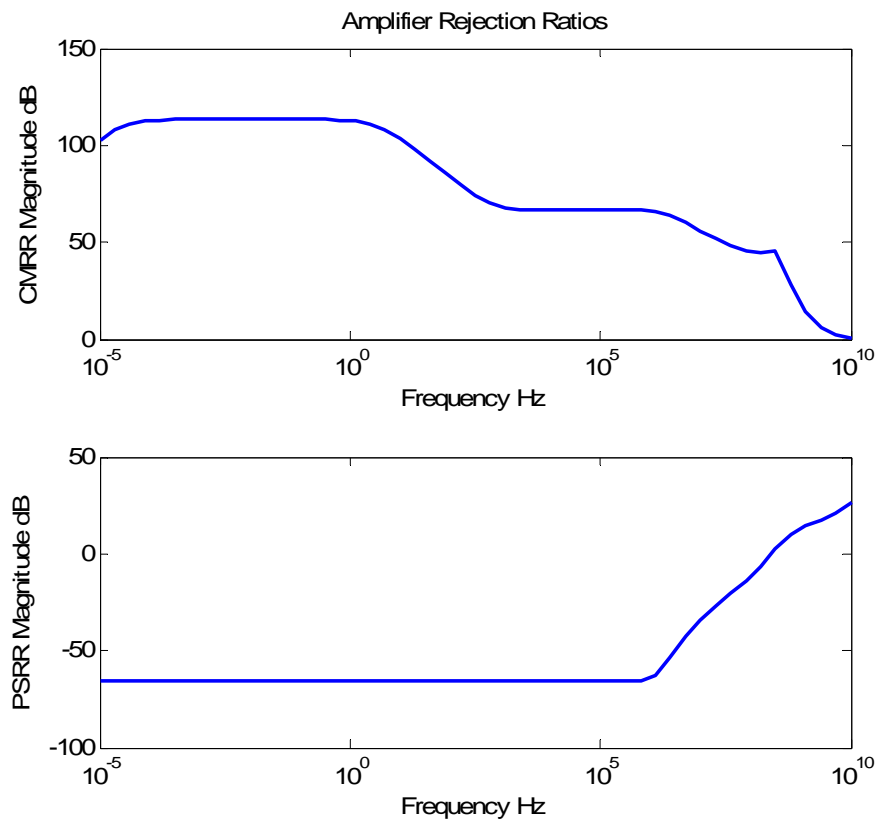
Figure A.6: CMRR and PSRR for Class AB Amplifier

Slew Rate:

Slew rate was measured using the configuration in Figure A.7. A 20 kHz, 2.5Vpp square wave with a rising and falling edge of 1ps was applied at the input. At the output, two points along the rising edge were measured to determine the slew rate of 12.94V/us.
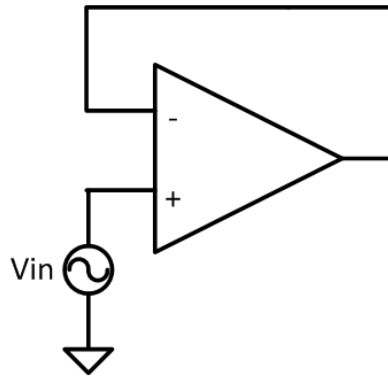
Figure A.7: Simulation configuration for slew rate measurement

Gain Bandwidth:

The GBW was measured using the configuration in Figure A.7 and was simulated to be ~12MHz.
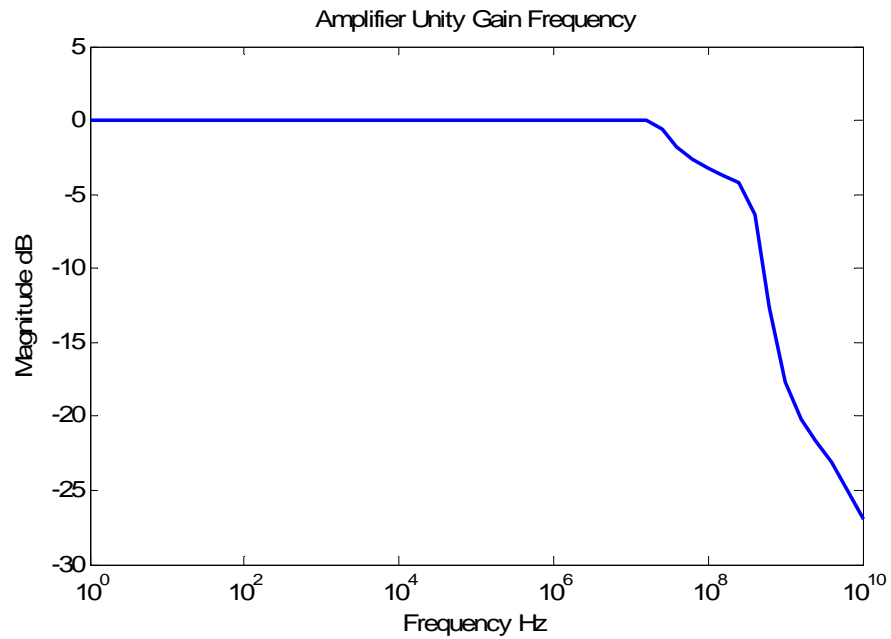
Figure A.8: Class AB Amplifier Gain Bandwidth

Noise:

For the input noise simulation, the circuit seen in Figure A.1 was used. The input referred voltage noise was integrated from 10uHz to the unity gain frequency to obtain the RMS value of 50.5uV$_{RMS}$.
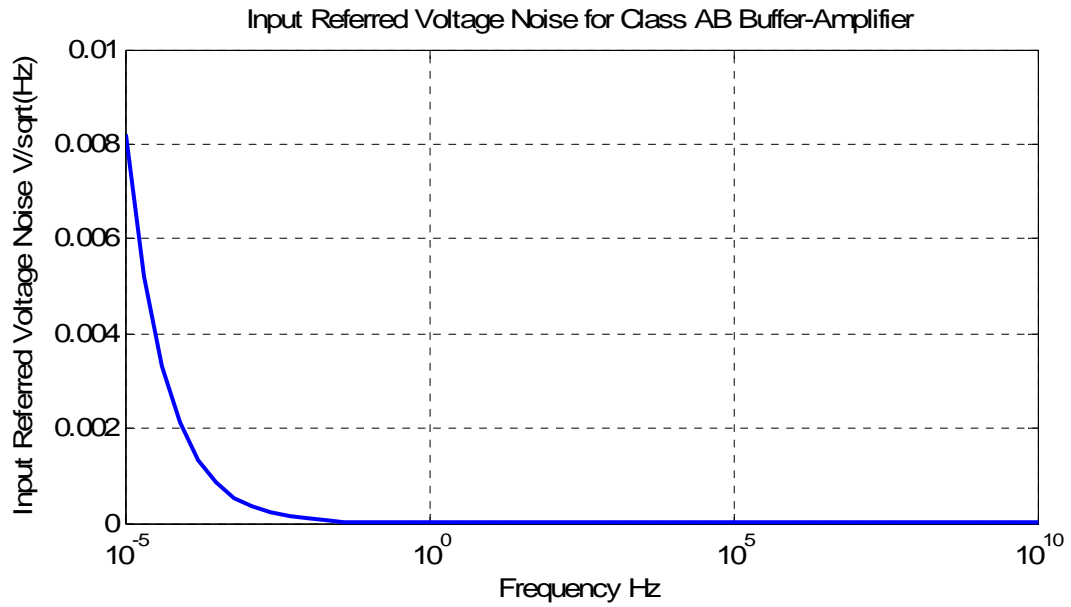
Figure A.9: Input Referred Voltage Noise for Class AB Amplifier

Short Circuit Current:

Short circuit current was simulated by connecting the amplifier in unity gain configuration and shorting the output to virtual ground. The input was stepped from 0 to 2.5V and the maximum current sourced/sunk by M15 and M16 of Figure 2.7 were plotted.

M15 Drain Current

M16 Drain Current
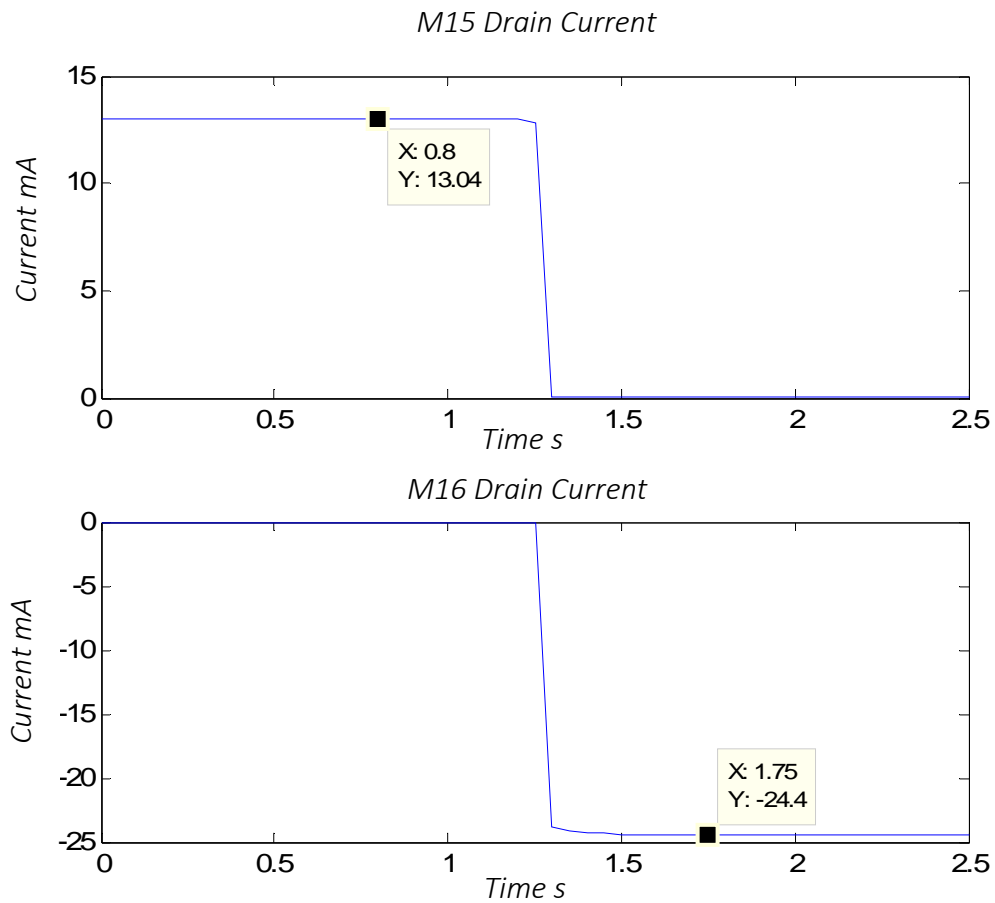
Figure A.10: Short Circuit Current. Input voltage is stepped from 0 to 2.5V at 1.25s.

Swing:

For swing determination, the amplifier was connected in unity gain configuration and connected to 200Ω and 1kΩ loads sequentially. The input was stepped from 0 to 2.5 V and the output voltage was plotted. For a 200Ω load the swing was 1.6V and 2V with a 1kΩ load.
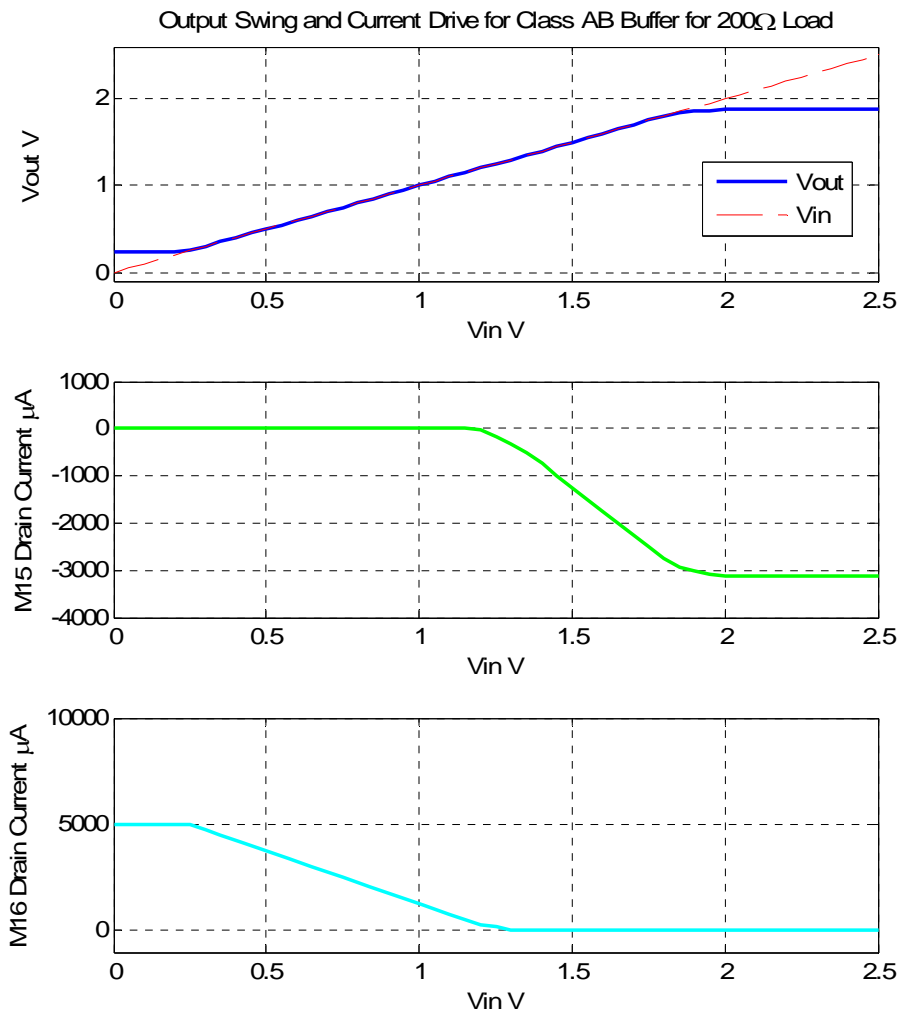
Figure A.11: Class AB Amplifier Swing for 200Ω Load

Appendix B: Class-AB Amplifier Noise Requirements for TIA

Leaving a margin on the maximum input range and the minimum detectible current, let us assume a desired current range of ±200uA of current with a minimum sensitivity of 50nA. The maximum achievable transimpedance gain (R_f) without saturating the amplifier is 6kΩ, given by (B1).

$$R_f = \frac{1.25V}{200uA} = 6000\Omega \qquad \text{(B1)}$$

To resolve 50nA, the input referred current noise (i_{ni}) must be less than this value, resulting in the requirement provided in (B2). This necessitates that the amplifier has an input referred voltage noise less than $89nV^2$ over the bandwidth, derived in (B4).
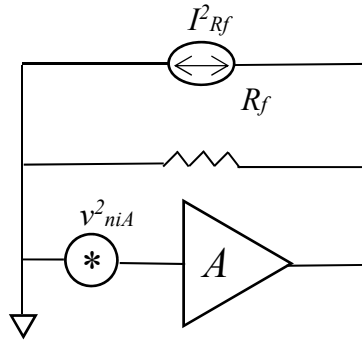
Figure B.1: Noise Model for Resistive Feedback TIA

$$i_{ni}^2 = \frac{v_{niA}^2}{Rf^2} + I_{Rf}^2 < 50nA \qquad \text{(B2)}$$

Here $v^2{}_{niA}$ is the input referred voltage noise of the class AB amplifier and $I^2{}_{Rf}$ is the resistor current noise model given by (B3).

$$I_{Rf}^2 = \frac{4kT}{R_f} \qquad \text{(B3)}$$

$$v_{niA}^2 < \left((50nA)^2 - \frac{4kT}{R_f} \right) * R_f^2 = 89nV^2 \qquad \text{(B4)}$$

$$\rightarrow v_{niA_{RMS}} = 300uV_{RMS} \qquad \text{(B5)}$$

Additionally, a 6kΩ transimpedance would result in a 300uV voltage change at the output of the amplifier for the 100nA input. This would require an ADC resolution of 14bits assuming the same 2.5V full scale input given by (B6).

$$ADC\ Resolution = \left\lceil \log_2 \left(\frac{2.5}{300\mu V} \right) \right\rceil = 14bits \qquad \text{(B6)}$$

Appendix C: Variable Gain TIA Transimpedance Measurement
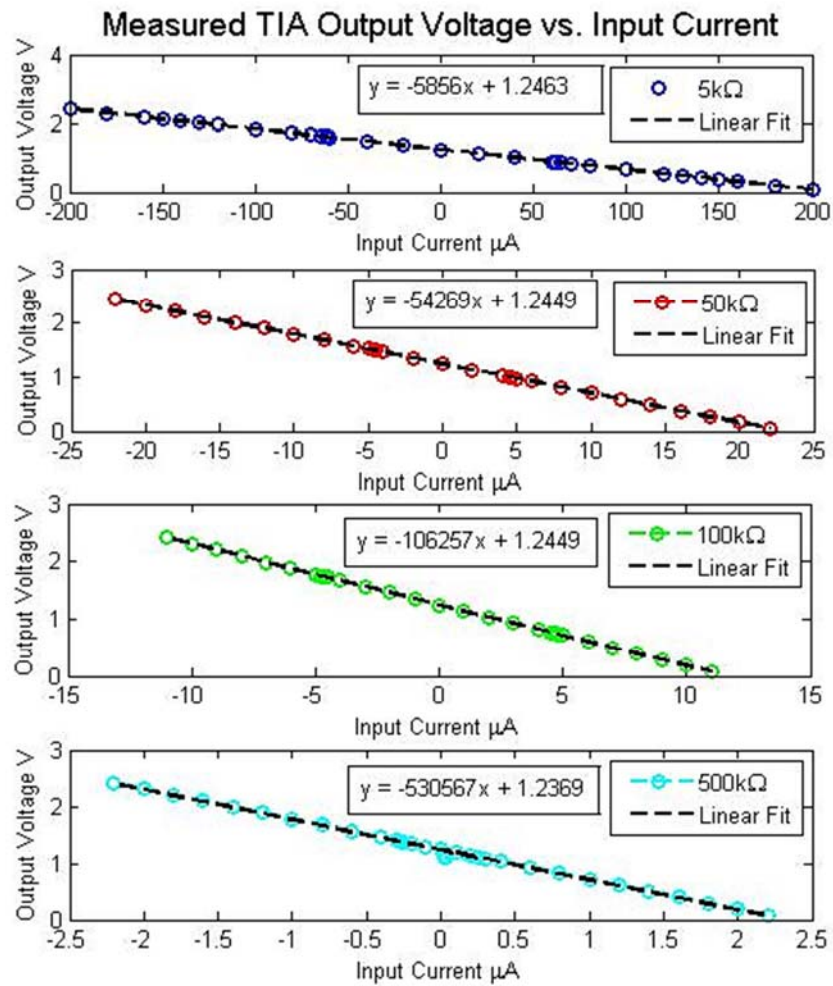
Figure C.1: Transimpedance amplifier output voltage vs. input current with capacitive load for four transimpedance values

Appendix D: Potentiostat Board Layout
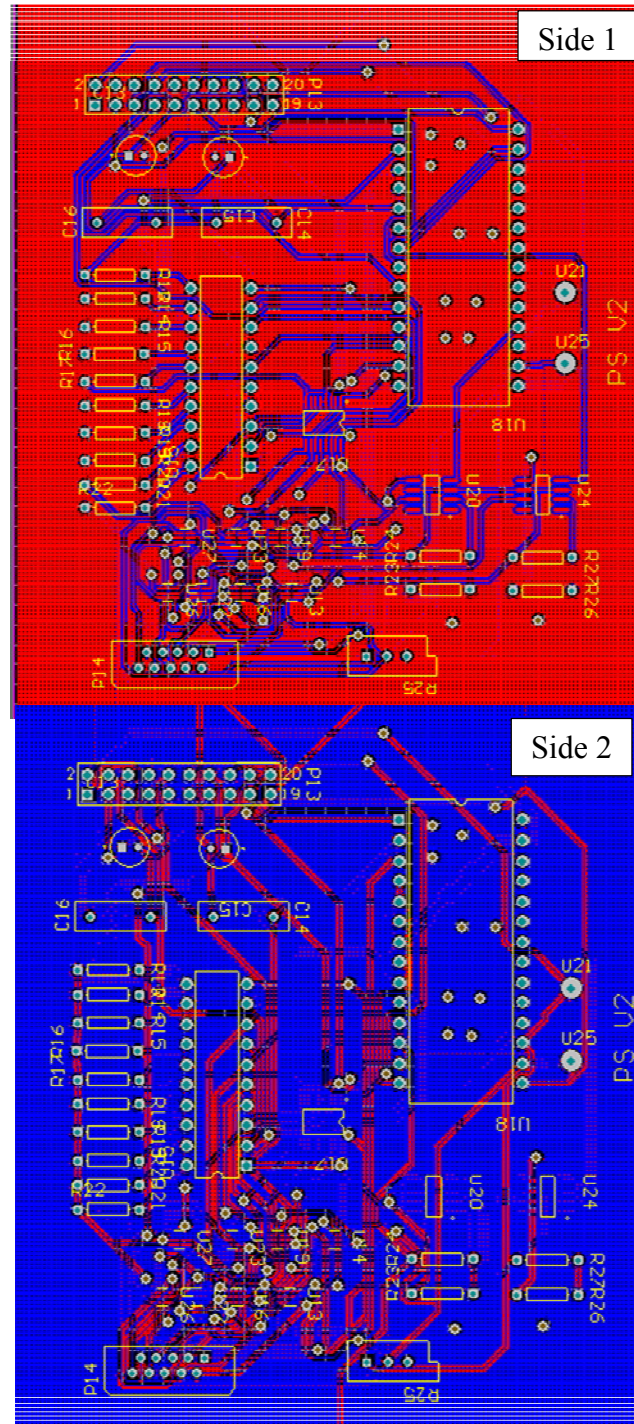
Figure D.1: Data Acquisition PCB Layout

Appendix E: Publications

Conference

- **Punjiya, Meera**, Pooria Mostafalu, and Sameer Sonkusale. "Low-cost paper-based electrochemical sensors with CMOS readout IC." In *2014 IEEE Biomedical Circuits and Systems Conference (BioCAS) Proceedings*, pp. 324-327. IEEE, 2014.

- **Punjiya, Meera**, Chung Hee Moon, and Sameer Sonkusale. " Multi-analyte Paper-Analytical-Devices (PAD) with CMOS Integration for Point-of-Care Diagnostics." In *2016 IEEE International Symposium on Circuits and Systems Conference (ISCAS) Proceedings*. IEEE, 2016.

- Mostafalu, P., S. Mostafalu, J. Mann, **M. Punjiya**, and S. Sonkusale. "Highly selective electrochemical approach for detection of DA, AA and 5-HT using material diversity with chemometrics on paper." In *2015 Transducers-2015 18th International Conference on Solid-State Sensors, Actuators and Microsystems (TRANSDUCERS)*, pp. 1479-1482. IEEE, 2015.

Works Cited

[1]   A. W. Martinez, S. T. Phillips and G. Whitesides, "Diagnostics for the developing world: microfluidic paper-based analytical devices.," *Analytical Chemistry,* vol. 82, no. 1, pp. 3-10, 2009.

[2]   R. W. Peeling, K. K. Holmes, D. Mabey and A. Ronald, "Rapid tests for sexually transmitted infections (STIs): the way forward," *Sexually Transmitted Infections,* vol. 82, no. 5, pp. v1-6, 2006.

[3]   H. Kettler, K. White and S. Hawkes, "Mapping the landscape of diagnostics for sexually transmitted infections: key findings and recommendations," World Health Organization, Geneva, 2004.

[4]   J. C. Cunningham, P. R. DeGregory and R. M. Crooks, "New Functionalities fo Paper-based Sensors Lead to Simplified User Operation, Lower Limits of Detection and New Applications," *Annual Review of Analytical Chemistry,* vol. 9, no. 4, pp. 1-20, 2016.

[5]   A. W. Martinez, S. T. Phillips, J. M. Butte and M. G. Whitesides, "Patterned Paper as a Platform for Inexpensive, Low-Volume, Portable Bioassays," *Angew. Chem. Int. Ed.,* vol. 46, pp. 1318-1320, 2007.

[6]   W. Dungchai, O. Chailapakul and C. S. Henry, "Electrochemical Detection for Paper-Based Microfluidics," *Analytical Chemistry,* vol. 81, no. 14, pp. 5821-5826, 2009.

[7]   Y. Lu, W. Shi, L. Jiang, J. Qin and B. Lin, "Rapid prototyping of paper-based microfluidics with wax for low-cost portable assay," *Electrophoresis,* vol. 30, pp. 1497-1500, 2009.

[8]   E. Carrilho, A. W. Martinez and G. M. Whitesides, "Understanding Wax Printing: A Simple Micropatterning Process for Paper-Based Microfluidics," *Analytical Chemistry,* vol. 81, pp. 7091-7095, 2009.

[9]   H. Liu and R. M. Crooks, "Three-Dimensional Paper Microfluidic Devices Assembled Using the Principals of Oragami," *Journal of the American Chemical Society,* vol. 133, pp. 17564-17566, 2011.

[10] C. Renault, X. Li, S. E. Fosdick and R. M. Crooks, "Hollow-Channel Paper Analytical Devices," *Analytical Chemistry,* vol. 85, p. 7976, 2013.

[11] F. Scholz, Electroanalytical Methods, Germany: Springer, 2002.

[12] D. Harvey, "Family Tree for Interfacial Electrochemical Techniques," 31 July 2013. [Online]. Available: http://community.asdlib.org/imageandvideoexchangeforum/2013/07/31/family-tree-for-interfacial-electrochemical-techniques/. [Accessed 10 July 2016].

[13] P. T. Kissenger and W. R. Heineman, "Cyclic Voltammetery," *Journal of Chemical Education,* vol. 60, p. 702, 1983.

[14] G. A. Mabbot, "An introduction to cyclic voltammetry," *Journal of Chemical Education,* vol. 60, no. 9, p. 697, 1983.

[15] M. Ciobanu, J. P. Wilburn, M. L. Krim and D. E. Cliffel, "Fundamentals," in *Handbook of Electrochemistry*, Amsterdam, Elsevier, 2007, pp. 3-29.

[16] Z. Nie, C. A. Gong, J. Gong, X. Chen, A. Kumachev, A. Martinez and G. Whitesides, "Electrochemical sensing in paper-based microfluidic devices," *Lab on a Chip,* vol. 10, no. 4, pp. 477-483, 2010.

[17] Gamry Instruments, "Potentiostat Fundamentals," Gamry Instruements, 2016. [Online]. Available: http://www.gamry.com/application-notes/instrumentation/potentiostat-fundamentals/. [Accessed 5 July 2016].

[18] K. Murari, M. Stanacevic, G. Cauwenberghs and N. Thakor, "Widerange, picoampere-sensitivity multichannel VLSI potentiostat for neurotransmitter sensing," *IEEE Engineering in Medicine and Biology,* vol. 24, no. 6, pp. 23-29, 2005.

[19] M. M. Ahmadi and G. A. Jullien, "Current-mirror-based potentiostats for three-electrode amperometric electrochemical sensors," *IEEE Transactions of circuits and systems,* vol. 56, no. 7, pp. 1339-1348, 2009.

[20] H. S. Narula and J. G. Harris, "A time-based VLSI potentiosat for ion current measurements," *IEEE sensors journal,* vol. 6, no. 2, 2006.

[21] A. J. Bard, B. Parsons and J. Jordon, Standard Potentials in Aqueous Solutions, New York: Dekker, 1985.

[22] G. Milazzo, S. Caroli and V. K. Sharma, Tables of Standard Electrode Potentials, London: Wiley, 1978.

[23] A. A. Ensafi, M. Taei, T. Khayamian and A. Arabzadeh, "Highly selective determination of ascorbic acid, dopamine, and uric acid by differential pulse voltammetry using poly (sulfonazo III) modified glassy carbon

electrode," *Sensors and Actuators B: Chemical ,* vol. 147, no. 1, pp. 213-221, 2010.

[24] M. Santhiago, J. B. Wydallis, L. T. Kubota and C. S. Henry, "Construction and electrochemical characterization of microelectrodes for improved sensitivity in paper-based analytical devices.," *Analytical Chemistry,* vol. 85, no. 10, pp. 5233-5239, 2013.

[25] H. Liu and R. M. Crooks, "Paper-Based Electrochemical Sensing Platform with Integral Battery and Electrochromic Read-Out," *Analytical Chemistry,* vol. 84, no. 5, pp. 2528-2532, 2012.

[26] E. Daftsis, N. Pagalos, A. Jannakoudakis, P. Jannakoudakis, E. Theodoridou, R. Rashkov, M. Loukaytsheva and N. Atanassov, "Preparation of a Carbon Fiber-Nickel-Type Material and Investigation of the Electrocatalytic Acvitivy for Hydrogen Evolution Reaction," *Journal of the Electrochemical Society,* vol. 150, no. 11, pp. C787-C793, 2003.

[27] T. Fujimoto and K. Awaga, "Electric-double-layer field-effect transistors with ionic liquids," *Physical Chemistry Chemical Physics,* vol. 15, no. 23, pp. 8983-9006, 2013.

[28] W. Franks, I. Schenker, P. Schmutz and A. Hierlemann, "Impedance Characterization and Modeling of Elec95-trodes for Biomedical Applications," *IEEE Transactions on Biomedical Engineering,* vol. 52, no. 7, pp. 1295-1302, 2005.

[29] Z. Jovanovic, G.-O. Buica, V. Miskovic-Stankovic, E.-M. Ungureanu and C.-A. Amarandei, "Electrochemical impedance spectroscopy investigations on glassy carbon electrodes modified with poly (4-azulen-1-yl-2,6-bis(2-thienyl)pyridine)," *U.P.B. Sci. Bull., Series B,* vol. 75, no. 1, pp. 125-134, 2013.

[30] S.-y. Shi, Z.-h. Fang and J.-r. Ni, "Electrochemial impedance spectroscopy of marmatite-carbon paste electrode in the presence and absence of Adicithiobacillus ferroxidans," *Electrochemistry Communications,* vol. 7, no. 11, pp. 1177-1182, 2005.

[31] Y. Fan , H. K. Embabi and E. Sanchez-Sinencio, "Low-voltage class AB buffers with quiscient current control," *IEEE Journal of Solid State Circuits,* vol. 33, no. 6, pp. 915-920, 1998.

[32] P. R. Gray and R. G. Meyer, "MOS operational amplifier design- a tutorial overview," *IEEE Journal of Solid State Circuits,* vol. 17, no. 6, pp. 969-982, 1982.

[33] S. Pernici, G. Nicollini and Castello, "A CMOS low-distortion fully differential power amplifier with double nested Miller compensation," *IEEE Journal of Solid State Circuits,* vol. 28, pp. 758-763, 1993.

[34] M. H. Nazari, H. Mazhab-Jafari, L. Leng, A. Guenther and R. Genov, "CMOS neurotransmitter microarray: 96-channel integrated potentiostat with on-die microsensors.," *IEEE transactions on biomedical circuits and systems,* vol. 7, no. 3, pp. 338-348, 2013.

[35] J. Rothe, O. Frey, A. Stettler, Y. Chen and A. Hierlemann, "Fully Integrated CMOS Microsystem for Electrochemical Measurements on 32x32 Working Electrodes at 90 frames per second," *Analytical Chemistry,* vol. 86, no. 13, pp. 6425-6436, 2015.

[36] L. Zuo, S. K. Islam, I. Mahbub and F. Quaiyum, "A Low-Power 1-V Potentiostat for Glucose Sensors.," *IEEE Transactions on Circuits and Systems II: Express Briefs,* vol. 62, no. 2, pp. 204-208, 2015.

[37] C.-Y. Huang, "Design and implementation of a voltammetry potentiostat with wide dyanmic current range measurement for electrochemical biosensors," *Analog Integr Circ Sig Process,* vol. 81, pp. 205-214, 2014.

[38] T. Luo, H. Wang, H. Song and J. B. Christen, "CMOS-based on-chip electrochemical sensor.," *2014 IEEE Biomedical Circuits and Systems Conference (BioCAS) Proceedings,* vol. IEEE, no. 2014, pp. 336-339, 2014.

[39] S. Hwang and S. Sonkusale, "CMOS VLSI potentiostat for portable environmental sensing applications.," *IEEE Sensors Journal ,* vol. 10, no. 4, pp. 820-821, 2010.

[40] R. P. Obermayr, C. Temml, G. Gutjahr, M. Knechtelsdorfer, R. Oberbauer and R. Klauser-Braun, "Elevated uric acid increases the risk for kidney disease," *Journal of the American Society of Nephrology,* vol. 19, no. 12, pp. 2407-2413, 2008.

[41] B. C. Martin, J. H. Warram, A. S. Krolewski, J. S. Soeldner, C. R. Kahn and R. N. Bergman, "Role of glucose and insulin resistance in development of type 2 diabetes mellitus: results of a 25-year follow-up study.," *The Lancet,* vol. 340, no. 8825, pp. 925-929, 1992.

[42] C. Chen, Q. Xie, D. Yang, H. Xiao, Y. Fu, Y. Tan and S. Yao, "Recent advances in electrochemical glucose biosensors: a review," *RSC Advances,* vol. 3, no. 14, pp. 4473-4491, 2013.

[43] W. Jia, A. J. Bandodkar, G. Valdes-Ramirez, J. R. Windmiller, Z. Yang, J. Ramirez and J. Wang, "Electrochemical tattoo biosensors for real-time noninvasive lactate monitoring in human perspiration," *Analytical Chemistry,* vol. 85, no. 14, pp. 6553-6560, 2013.

[44] S. Qi, B. Zhao, H. Tang and X. Jiang, "Determination of ascorbic acid, dopamine, and uric acid by a novel electrochemical sensor based on pristine graphene," *Electrochimica Acta,* vol. 161, pp. 395-402, 2015.

[45] D. Freeman, D. Boecker and D. Alden, "Method and apparatus for analyte detecting device". United States Patent US 9386944 B2, 10 April 2009.

[46] M. Sherman, "How do blood glucose meters work?," December 2006. [Online]. Available: https://uwaterloo.ca/chem13news/sites/ca.chem13news/files/uploads/files/343_dec_2006_pages_5-6.pdf. [Accessed July 2016].

[47] K. Jackowska and P. Krysinski, "New Trends in the electrochemical sesning of dopamine," *Analytical Bioanalytical Chemistry,* vol. 405, p. 3753–3771, 2013.

[48] J.-B. Raoof, R. Ojani and S. Rashid-Nadimi, "Voltammetric determination of ascorbic acid and dopamine in the same sample at the surface of a carbon paste electrode modified with polypyrrole/ferrocyanide films," *Electrochimica Acta,* vol. 50, no. 24, pp. 4694-4698, 2005.

[49] S.-M. Chen and K.-T. Peng, "The electrochemical properties of dopamine, epinephrine, norepinephrine, and their electrocatalytic reactions on cobalt(II) hexacyanoferrate films," *Journal of Electroanalytical Chemistry,* vol. 547, no. 8, pp. 179-189, 2003.

[50] Z. Jin, Y. Su and Y. Duan, "An improved optical pH sensor based on polyaniline," *Sensors and Actuators B: Chemical,* vol. 71, no. 1, pp. 118-122, 2000.

[51] S. K. Manohar, C. Fafadia, N. Saran and R. Rao, "Faradiac effects in all-oragnic transistors," *Journal of Applied Physics,* vol. 094501, p. 103, 2008.

[52] Z. Nie and F. Diess, "Integration of paper-based microfluidic devices with commercial electrochemical readers," *Lab on a Chip,* vol. 10, no. 22, pp. 3163-3169, 2010.

[53] P. Mostafalu, *Nano-enabled sensors, electronics and energy source on polymer, paper and thread substrates,* Boston: ProQuest, 2016.

[54] P. Mostafalu, A. M, K. Alberti, Q. Xu, A. Khademhosseini and S. Sameer, "A toolkit of thread-based microfluidics, sensors, and electronics for 3D tissue embedding for medical diagnostics," *Microsystems & Nanoengineering,* vol. 2, 2016.

[55] R. O. Kandara, N. Jenkinson and C. E. Banks, "Characterisation of commercially available electrochemical sensing platforms," *Sensors and Actuators B: Chemical,* vol. 138, no. 2, pp. 556-562, 2009.

[56] R. B. Kawde and K. S. V. Santhanam, "An in vitro electrochemical sensing of dopamine in the presence of ascorbic acid.," *Bioelectrochemistry and bioenergetics,* vol. 38, no. 2, pp. 405-409, 1995.

[57] T. Choudhary, G. P. Rajamanickam and D. Dendukuri, "Woven electrochemical fabric-based test sensors (WEFTS): a new class of multiplexed electrochemical sensors," *Lab on a Chip,* vol. 15, no. 9, pp. 2064-2072, 2016.

[58] A. Ciszewski and G. Milczarek, "Polyeugenol-modified platinum electrode for selective detection of dopamine in the presence of ascorbic acid.," *Analytical Chemistry,* vol. 71, no. 5, pp. 1055-1061, 1995.

[59] S. P. Kounaves, "Voltammetric Techniques," in *Handbook of Instrumental Techniques for Analytical Chemistry*, Prentice Hall, 1997, pp. 709-725.